

Massive open star clusters using the VVV survey^{★,★★}

I. Presentation of the data and description of the approach

A.-N. Chené^{1,2}, J. Borissova^{1,3}, J. R. A. Clarke^{1,4}, C. Bonatto⁵, D. J. Majaess⁶, C. Moni Bidin², S. E. Sale^{1,7}, F. Mauro², R. Kurtev¹, G. Baume⁸, C. Feinstein⁸, V. D. Ivanov⁹, D. Geisler², M. Catelan^{3,7}, D. Minniti^{3,7,10,11}, P. Lucas⁴, R. de Grijs¹², and M. S. N. Kumar¹³

¹ Departamento de Física y Astronomía, Universidad de Valparaíso, Av. Gran Bretaña 1111, Playa Ancha, Casilla 5030, Chile
e-mail: andrenicolas.chene@gmail.com

² Departamento de Astronomía, Universidad de Concepción, Casilla 160-C, Chile

³ The Milky Way Millennium Nucleus, Av. Vicuña Mackenna 4860, 782-0436 Macul, Santiago, Chile

⁴ University of Hertfordshire, Hatfield, AL10 9AB, UK

⁵ Universidade Federal do Rio Grande do Sul, Departamento de Astronomia CP 15051, RS, Porto Alegre, 91501-970, Brazil

⁶ Saint Marys University, Halifax, Nova Scotia, Canada

⁷ Pontificia Universidad Católica de Chile, Facultad de Física, Departamento de Astronomía y Astrofísica,
Av. Vicuña Mackenna 4860, 782-0436 Macul, Santiago, Chile

⁸ Facultad de Ciencias Astronómicas y Geofísicas (UNLP), Instituto de Astrofísica de La Plata (CONICET, UNLP),
Paseo del Bosque s/n, La Plata, Argentina

⁹ European Southern Observatory, Ave. Alonso de Cordova 3107, Casilla 19, Chile

¹⁰ Vatican Observatory, V00120 Vatican City State, Italy

¹¹ Department of Astrophysical Sciences, Princeton University, Princeton NJ 08544-1001

¹² Kavli Institute for Astronomy and Astrophysics, Peking University, Yi He Yuan Lu 5, Hai Dian District, Beijing 100871, PR China

¹³ Centro de Astrofísica da Universidade do Porto, Rua das Estrelas, 4150-762 Porto, Portugal

Received 17 February 2012 / Accepted 26 June 2012

ABSTRACT

Context. The ESO Public Survey “VISTA Variables in the Vía Láctea” (VVV) provides deep multi-epoch infrared observations for unprecedented 562 sq. degrees of the Galactic bulge, and adjacent regions of the disk.

Aims. The VVV observations will foster the construction of a sample of Galactic star clusters with reliable and homogeneously derived physical parameters (e.g., age, distance, and mass, etc.). In this first paper in a series, the methodology employed to establish cluster parameters for the envisioned database are elaborated upon by analysing four known young open clusters: Danks 1, Danks 2, RCW 79, and DBS 132. The analysis offers a first glimpse of the information that can be gleaned from the VVV observations for clusters in the final database.

Methods. Wide-field, deep JHK_s VVV observations, combined with new infrared spectroscopy, are employed to constrain fundamental parameters for a subset of clusters.

Results. Results are inferred from VVV near-infrared photometry and numerous low resolution spectra (typically more than 10 per cluster). The high quality of the spectra and the deep wide-field VVV photometry enables us to precisely and independently determine the characteristics of the clusters studied, which we compare to previous determinations. An anomalous reddening law in the direction of the Danks clusters is found, specifically $E(J - H)/E(H - K_s) = 2.20 \pm 0.06$, which exceeds published values for the inner Galaxy. The G305 star forming complex, which includes the Danks clusters, lies beyond the Sagittarius-Carina spiral arm and occupies the Centaurus arm. Finally, the first deep infrared colour-magnitude diagram of RCW 79 is presented, which reveals a sizeable pre-main sequence population. A list of candidate variable stars in G305 region is reported.

Conclusions. This study demonstrates the strength of the dataset and methodology employed, and constitutes the first step of a broader study which shall include reliable parameters for a sizeable number of poorly characterised and/or newly discovered clusters.

Key words. open clusters and associations: general – infrared: stars – surveys

1. Introduction

It is commonly accepted that the majority of stars with masses $\geq 0.50 M_\odot$ form in clustered environments (e.g.

Lada & Lada 2003; de Wit et al. 2005), rather than individually. Our location within our own Galaxy gives us a unique perspective from which we can study star clusters in great detail and such studies have important implications for our understanding of the formation of large galaxies in general.

Estimates indicate that the Milky Way (MW) presently hosts 23 000–37 000 or more star clusters (Portegies Zwart et al. 2010). However, only 2135 open clusters have been identified (according to the 26 Jan. 2012 version of Dias et al. 2002), which constitute a sample affected by several well known selection effects (as with globular clusters; Ivanov et al. 2005). Less

* Based on observations made with NTT telescope at the La Silla Observatory, ESO, under programme ID 087.D-0490A, and with the Clay telescope at the Las Campanas Observatory under programme CN2011A-086. Also based on data from the VVV survey observed under program ID 172.B-2002.

** Tables 1, 5 and 6 are available in electronic form at
<http://www.aanda.org>

than half of these clusters have actually been studied, and this subset suffers from further selection biases. Extending this current sample towards the Milky Way's highly obscured central region would provide unique insight into the formation, evolution, and dissipation of open clusters in the Galactic environment. To achieve this goal, we are using the unprecedented deep infrared data from the VISTA Variables in the Vía Láctea (VVV) survey (Minniti et al. 2010; Saito et al. 2012), one of the six ESO Public Surveys operating on the new 4-m Visible and Infrared Survey Telescope for Astronomy (VISTA). We are in the process of building a large sample of star clusters (including many discovered by our group; Borissova et al. 2011; Bonatto et al., in prep.), that are practically invisible in the optical bands. The strength of this sample will lie in the homogeneity of the data (i.e. all observed with the same instrument and set-up) and analysis employed. From which, we will estimate clusters' physical parameters, including: angular sizes, radial velocities (RVs), reddening, distances, masses, and ages. Moreover, as pointed out by Majaess et al. (2012), VVV photometry allows these parameters to be determined with unprecedented accuracy for highly obscured clusters.

As a first step, we are focusing our efforts on young open clusters in their first few Myrs. During this period, which corresponds to Phase *I* in the recent classification of Portegies Zwart et al. (2010), stars are still forming and the cluster contains a significant amount of gas. The evolution of the cluster during this phase is governed by a complex mixture of gas dynamics, stellar dynamics, stellar evolution, and radiative transfer, and is currently not completely understood (Elmegreen 2007; Price & Bate 2009). Thus many basic (and critical) cluster properties, such as the duration and efficiency of the star-formation process, the cluster survival probability and the stellar mass function at the beginning of the next phase are uncertain.

In this paper, we present a first sub-sample of 3 known young open clusters, studying them with both VVV colour-magnitude diagrams (CMDs) and low resolution near-infrared spectroscopy of the brightest stellar members. These clusters are RCW 79, already studied by Martins et al. (2010), and Danks 1 and Danks 2, discussed by Davies et al. (2012). We aim to describe our approach and present a first glimpse of the data quality. We detail our approach for determining the physical parameters of clusters observed with VVV, using previous works as references. As DBS 132 is located close to Danks 1 and Danks 2, we also examine its CMDs and derive some preliminary cluster parameters.

We begin by presenting the data in Sect. 2, and relating our method and evaluating the accuracy of our work in Sect. 3. Subsequently, we describe the stellar variability detected in the clusters and their surroundings in Sect. 4. Then, in Sect. 5 we compare our results with previous studies and briefly discuss the characteristics of the star-forming regions in which the clusters are situated. Before concluding by summarising this work in Sect. 6.

2. Observations

2.1. Photometry

2.1.1. VVV data and photometry extraction

We downloaded, from the VISTA Science Archive (VSA) website¹, the stacked images of the individual 2048×2048 pixel exposures containing the three clusters presented in this paper. Danks 1 and Danks 2 both appear in VVV field d084, whilst

RCW 79 falls in VVV field d086. These fields were observed twice in the $ZYJHK_s$ bands on 7 to 29 March 2010 (d084), and 18 March to 4 April 2010 (d086), with the VIRCAM camera mounted on the VISTA 4 m telescope at Paranal Observatory (Emerson & Sutherland 2010). The images were then reduced at CASU² by the VIRCAM pipeline v1.1 (Irwin et al. 2004). The total exposure time of each of these images was 40 s, with 2 images per filter, on average. For a detailed description of the observing strategy see Minniti et al. (2010); Saito et al. (2012) provide further details about VVV data.

During the observations the weather conditions fell within all the survey constraints for seeing, airmass, and Moon distance (Minniti et al. 2010) and the quality of the data was satisfactory. JHK_s true colour images of the three clusters are shown in Fig. 1. Additional 8 s K_s -band images were also obtained in order to find and monitor variable stars in these fields. The dates, airmass, seeing, ellipticity and observation quality grade are all listed in Table 1.

The VVV-SkZ_pipeline (Mauro et al. 2012) was employed to determine stellar photometry from the images. The VVV-SkZ_pipeline is automated, based on ALLFRAME (Stetson 1994) and optimised for PSF photometry of VVV data. The VVV-SkZ_pipeline uses single pointing images, called paw prints (covering 0.59 sq. deg). CASU aperture photometry is available for paw prints as well as tiles, which are the combination of 6 pawprints giving a full 1.64 sq. deg combined image (see Saito et al. 2012 for more details about pawprints and tiles). For PSF photometry we only use paw prints as sources on a tile have PSF shapes that are too difficult to model, due to the variable PSF across each combined tile. In such conditions PSF fitting does is no more accurate than simple aperture photometry. To take into account the variable PSF, the VVV-SkZ_pipeline simply allows the PSF to vary quadratically across the pawprints field-of-view.

The final product of the pipeline is an astrometric, flux calibrated star catalogue. PSF photometry produces many spurious detections close to defects on the detectors, in the border of the fields, in the core and on the speckles of saturated stars. These can be isolated when, for all sources, the photometric errors given in ALLFRAME's output are compared with the apparent magnitudes, since the error on the fit of fake detections tends to be comparatively high. The VVV-SkZ_pipeline finds the maximum of the error distribution per magnitude bin (typically 0.1 mag), and fits a polynomial function to get the photometric error as a function of magnitude. We then employ a sigma clipping algorithm to remove spurious detections: all detections showing a photometric error higher than 3σ are removed. One should note that the errors given by ALLFRAME are not the real photometric error, since it does not take into account all sources of error. For instance, it does not account for the correlation in the noise between adjacent pixels in infrared detectors.

Calibration in the VVV J -, H - and K_s -bands was done using 2MASS stars with $12.5 < J < 14.5$ mag, $11.5 < H < 13$ mag and $11 < K_s < 12.5$ mag (see Fig. 2). Stars brighter than $K_s \sim 12.5$ mag are saturated in the VVV disk area, however ALLFRAME uses the wings of the point-spread function of these stars to estimate their apparent magnitude, and we obtain a relative accuracy of 0.05 mag for stars up to mag = 9.0. For stars brighter than $K_s = 9.0$ mag we just adopted the 2MASS magnitudes. At the faint end a relative accuracy of 0.1 mag or better is achieved down to $J = 20.0$ mag or $K_s = 18.0$ mag. We did not correct the magnitudes of the 2MASS calibration stars into

¹ <http://horus.roe.ac.uk/vsa/>

² <http://casu.ast.cam.ac.uk/>

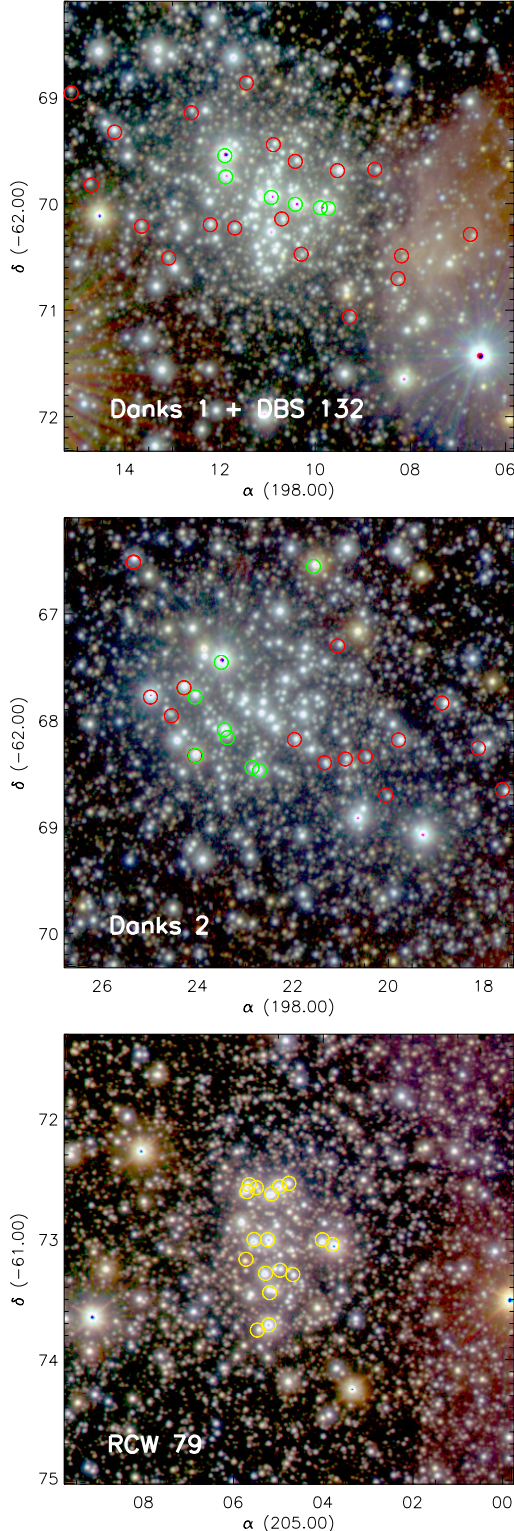


Fig. 1. JHK_s true colour images of the three clusters. Stars marked by circles were observed using near infrared spectrographs. In green are the stars observed using SofI at NTT and in red are the stars observed with MMIRS at the Clay telescope. The stars marked with a yellow circle in RCW 79 were already observed by Martins et al. (2010) and, hence, were not re-observed by us.

the VISTA photometric system, or apply any extinctions related terms (see below) unlike the procedure adopted by the VISTA Data Flow System pipeline at CASU. Thus our magnitudes differ from those in the catalogues produced by CASU which are

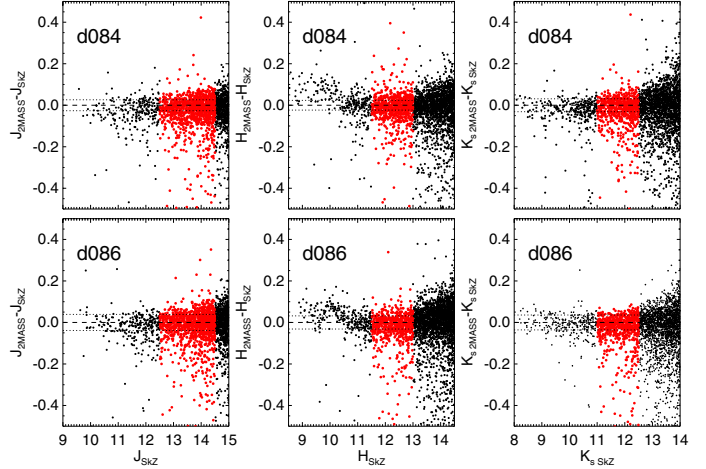


Fig. 2. Comparison between the VVV-SkZ_pipeline’s JHK_s photometry and that from the 2MASS catalogue. Since the VVV-SkZ_pipeline’s astrometric solution is based on the 2MASS catalogue, we were able to match most of the stars within a $1''$ -radius. Red, big circles are the stars within the magnitude intervals used for the flux calibration, i.e. $12.5 < J < 14.5$ mag, $11.5 < H < 13$ mag and $11 < K_s < 12.5$ mag. A dashed line shows where the VVV-SkZ_pipeline’s photometry perfectly matches the 2MASS values, and the dotted lines show the standard deviation of the points.

available through the VSA and via ESO³. We designate our VVV magnitudes in the 2MASS system as $M(VVV_{2MASS})$ to distinguish them from magnitudes for the same objects in the VISTA system, $M(VISTA)$. We opted to work in the 2MASS system rather than remaining in the natural VISTA system, as most of the models we are using in this study, and most of the other studies of massive clusters, employ the 2MASS photometric system.

For each of the 16 detectors in each pawprint our calibration of VVV data uses the 2MASS magnitude $M(2MASS)$ of stars with colours $\text{col}(2MASS)$ and the instrumental magnitudes $m(VVV)$ from the VVV-SkZ_pipeline psf fitting pipeline. It determines the two constants M_0 the zero-point and d the colour coefficient in the fit $M(2MASS) - m(VVV) = M_0 + d \text{col}(2MASS)$. The magnitudes of the VVV sources on the 2MASS system $M(VVV_{2MASS})$ are then found by inverting this equation. Our full transformation equations also include aperture correction and airmass effects.

Of course, transformations between two photometric systems depend on reddening. As we calibrate flux separately for each VIRCAM detector, we are effectively assuming, through our colour coefficient d , a mean reddening in each of those chips. One could use Schlegel et al. (1998)’s reddening maps, but this map’s spatial resolution is equivalent to nearly one VIRCAM chip and should provide similar results. Moreover, the use of these maps is also highly questionable at these latitudes as mentioned by Schlegel et al. (1998) themselves, since at low Galactic latitudes ($|b| < 5^\circ$), most contaminating sources have not been removed from their maps, and the temperature structure of the Galaxy is not well resolved. Furthermore, no comparisons between our predicted reddening from d and observed reddening have been made in these regions. One should note that the 2MASS photometry shows a dispersion higher than 0.1 mag for $K > 13$ mag.

³ http://archive.eso.org/wdb/wdb/adp/phase3_vircam/form

To calculate the completeness of our catalogue, we created Luminosity Functions (LFs) for the clusters, with a bin size of 0.5 K -band magnitudes. For each magnitude bin, we added artificial stars within the given magnitude ranges to the cluster image. The completeness was calculated by finding the recovery fraction of artificial stars per magnitude. The detection of the stars was done using daophot following a similar methodology as performed by the VVV-SkZ_pipeline.

2.1.2. Field star decontamination

To disentangle field and cluster stars we employed the statistical decontamination algorithm described in Bonatto & Bica (2010, and references therein), adapted to exploit the greater photometric depth of VVV. The algorithm first requires the identification of a comparison field. Depending on the projected distribution of individual stars, clusters or clumpy extinction, this may be a ring around the cluster or some other region selected in its immediate vicinity. The algorithm divides the full range of CMD magnitudes and colours into a grid of cells with axes along K_s , $(H - K_s)$ and $(J - K_s)$. Initial cell dimensions are $\Delta K_s = 1.0$ and $\Delta(H - K_s) = \Delta(J - K_s) = 0.2$ mag. However, sizes half and twice those values are also considered, together with shifts in the grid positioning by $\pm 1/3$ of the respective cell size along the 3 axes. Thus, 729 independent decontamination outputs were obtained for each cluster candidate. For each cell, the algorithm estimates the expected number density of member stars by subtracting the respective field star number-density⁴. Summing over all cells, each grid setup produces a total number of member stars N_{mem} and, repeating this procedure for the 729 different setups, we obtain the average number of member stars $\langle N_{\text{mem}} \rangle$. Each star is ranked according to the survival frequency after all runs, and only the $\langle N_{\text{mem}} \rangle$ highest ranked stars are taken as cluster members. A full description of the algorithm is given in Bonatto & Bica (2010). As a photometric quality constraint, the algorithm rejects stars with K_s or colour uncertainties greater than 0.1 mag.

2.2. Near-infrared spectroscopy

2.2.1. Observations

We collected spectra of 6 members of Danks 1 and 8 members of Danks 2, using the infrared spectrograph and imaging camera SofI in long-slit mode on the New Technology Telescope (NTT) at La Silla Observatory ESO, Chile. These stars are marked in Fig. 1 by green circles. Using the medium resolution grism in the 3rd order, we covered the whole K_s -band, 2.00–2.30 μm , with a resolution of $\Delta\lambda = 4.66 \text{ \AA/pix}$. We used a 1 arcsec slit, in order to match the seeing, which gives a resolving power of $R \sim 1320$. For optimal subtraction of the atmospheric OH emission lines, we used 60 arcsec nodding along the slit in an ABBA pattern: the star was observed before (A) and after (B) a first nod along the slit, then at position B a second time before returning to position A for a last exposure. All stars were observed using two slit positions per cluster. The position angle of the slit was chosen so that two or more stars were observed simultaneously. Total exposure time was 40 s for stars in Danks 1, and 160 s and 600 s for the brightest and the faintest stars in Danks 2, respectively. The total signal-to-noise ratio (S/N) per pixel ranges from 60 for the faintest stars to 150 for the brightest. Bright stars of spectral

type G were observed as a measure of the atmospheric absorption. These stars were selected to share the same airmass as the targeted clusters' stars during the middle of their observation. The spectra of the two stars HD 113376 (G3 V) and HD 120954 (G1 V) were obtained after the observations of the first and the second slit position on Danks 1 on 14 and 18 April 2011, respectively. Also, the star HD 119550 (G2 V) was observed just after the two slit positions on Danks 2 on 15 April 2011.

We also obtained a total of 38 spectra of stars within and in the vicinity of the star clusters Danks 1 and Danks 2, using the near-infrared spectrograph MMIRS in multi-object mode on the Clay telescope at Las Campanas Observatory on 2011 May 19, 20. These stars are indicated in Fig. 1 by red circles. Using the HK grism, we covered a spectral range of $\lambda\lambda = 1.25\text{--}2.45 \mu\text{m}$, with a resolution of $\Delta\lambda = 6.70 \text{ \AA/pix}$. We needed two slit-mask designs to observe all our targets of interest. Both used a slit-width of 0.5 arcsec, which gives a resolving power of $R \sim 1120$. As with the SofI data, nodding along the slits was used, but due to the small size of the slits, we only used 2 arcsec nodding in an ABCCBA pattern, which is similar to an ABBA pattern, but with third position along the slit. Individual exposure time was limited to 300 s to allow for accurate subtraction of the sky emission and the total exposure time was 2700 s for all stars. The average total S/N per pixel reached ranges from 100 to 200 for stars brighter than $K_s = 12.0$ mag and from 30 to 90 for stars fainter than $K_s = 12.0$ mag. The star HD 114012 (spectral type A0 V) was observed after the first mask as a measure of the atmospheric absorption.

Martins et al. (2010) obtained high quality NIR spectra of stars in RCW79. Hence, we use their spectra to complement our photometry.

2.2.2. Reduction and extraction

Before standard procedures could be applied to reduce the data, some initial processing steps were required to deal with peculiarities of the instruments we used. In the case of SofI spectra, we first had to correct for bad pixels, using the latest bad pixel mask available on the European Southern Observatory webpage⁵. Then correct for cross-talk, as described in the SofI User's Manual (Moorwood et al. 1998). With MMIRS spectra, which were obtained through "up the ramp" acquisition, a few more steps were needed. Each fits file consists of a data cube containing the non-destructive readout of the whole detector at every 5 s step. Hence, after subtracting the dark frame from the science data, one can collapse all readouts taken during an exposure into a single image by fitting a slope to the number of counts as a function of time for each pixel (as suggested on the MMIRS webpage⁶). By doing so, when the linearity and the saturation levels of each pixel are taken into account adequately, one corrects for cosmic rays and for saturated lines. The last step before running a standard reduction was to find, trace and cut the individual slits in the original image. The traces were fitted using a 4th-order polynomial fit and rectified before being cut. All steps described above were executed using custom-written Interactive Data Language (IDL) scripts.

Subsequent nodding observations were subtracted from one another to remove bias level and sky emission lines. The flat fielding, spectrum extraction and wavelength calibration of all

⁴ Photometric uncertainties are considered by computing the probability of a star of given magnitude and colour to be found in any cell (i.e., the difference of the error function computed at the cell borders).

⁵ http://www.eso.org/lasilla/instruments/sofi/tools/reduction/bad_pix.html

⁶ <http://hopper.sci.edu/wiki/mmri/MMTI/MMIRS/MMIRS+Pipeline>

spectra were executed in the usual way using **IRAF**⁷. Calibration lamp spectra (Xenon-Neon for SofI and Argon for MMIRS), taken at the beginning of each night, were used for wavelength calibration. The wavelength solution of each frame has an rms uncertainty of ~ 0.5 pixels for SofI spectra and 0.2 pixels for MMIRS spectra, which correspond to ~ 30 and ~ 20 km s $^{-1}$, respectively. Atmospheric absorption was corrected for with the **IRAF** task *telluric*. When a G-type star was used, it was first divided by a solar spectrum downloaded from the National Solar Observatory (Livingston & Wallace 1991) and resampled following the method described by Maiolino et al. (1996). When an A0 star was used, we first subtracted a fitted Voigt profile from the standard Br absorption features before running the task *telluric*.

Finally, all spectra were rectified using a low-order polynomial fit to a wavelength interval that was assumed to be pure continuum, i.e. without absorption or emission lines. Unfortunately, due to bad weather, observing was abruptly interrupted just before we could observe a telluric standard for the second mask at Las Campanas. Both masks were observed during different nights, but since they were observed at comparable airmasses (~ 1.2), we decided to use the same telluric standard for all spectra. Depending on how the weather conditions and the sky level were different during the two nights, this could have introduced uncertainties in the extraction of the spectra of the second mask, but nothing significant is observed. Indeed, one star was observed with both masks and, as one can see in Fig. 3, the two spectra are very similar. Figure 3 also shows the similarity of two spectra of another star observed using both SofI and MMIRs. Hence, our reduction and extraction methods can be trusted.

2.2.3. Spectral classification

The spectra of the stars in the area of the clusters Danks 1, Danks 2 and DBS2003 132 are plotted in Fig. 4. Preliminary spectral classifications were made using available catalogues of K -band spectra of objects with spectral types derived from optical studies (Morris et al. 1996; Figer et al. 1997; Hanson et al. 1996, 2005) as well as the spectral catalogues of Martins et al. (2007), Crowther et al. (2006), Liermann et al. (2009), Mauerhan et al. (2011) and Davies et al. (2012). The most prominent lines in our wavelength range are: Br γ (4–7) 2.1661 μm ; Br 10 (4–10) 1.737 μm ; Br 11 (4–11) 1.681 μm and Br 12 (4–12) 1.641 μm (all from the Brackett series); Pa β (3–5) 1.282 μm , from the Paschen series; HeI lines at 2.1127 μm ($3\text{p}^3\text{P}^0 - 4\text{s}^3\text{S}$, triplet), 1.702 μm ($1\text{s}^4\text{d}^3\text{D}^e - 1\text{s}^3\text{p}^3\text{P}^o$), 1.668 μm (4–11) and 1.722 μm (4–10); HeII lines at 2.188 μm (7–10) and 1.692 μm (12–7); the blend of CIII, NIII and OIII at 2.115 μm ; NIII $\lambda 2.103 \mu\text{m}$; CIV lines at 2.070 μm and 2.079 μm . All these lines were compared with the template spectra from the listed papers.

The equivalent widths (EWs) of the Br 11 (4–11) and HeI 1.702 μm lines of the spectral targets were measured, on the continuum normalised spectra, by the **IRAF** task *splot*. In general, we fit line profiles using a Gaussian with a linear background, in more complicated profiles we used the deblending function or Voigt profile fitting. The EW uncertainties were estimated taking into account the S/N of the spectra, the peak to continuum ratio of the line (see Bik et al. 2005) and the error from the telluric star

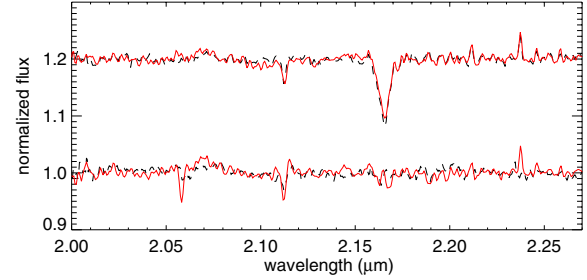


Fig. 3. Section of the K_s spectrum of two stars that were observed using different instruments and/or different slit masks. Obj2 (top) was observed with MMIRS using the first (solid, black line) and the second (dashed, red line) slit mask. Obj5 (bottom) was observed with NTT/SofI (solid, black line) and Clay/MMIRS (red, dashed line). An arbitrary shift in flux was applied for better visual representation.

subtraction (which was estimated to be ~ 10 –15% in the worst cases). The EWs of the emission lines are negative by definition. Their ratio was used for qualitative estimation of the spectral types of OB stars, using the calibrations given in Hanson et al. (1998).

In general, the spectra of most stars show the HeI lines and the Brackett series in absorption, which is typical for O and early B main sequence (MS) stars. Several stars, namely Obs. 1, 4, 19, 25, 26, 28 and 42, show only the Brackett series in absorption and are classified as later B – early A type stars. The stars Obj 3 and 21 present CO, MgI, Fe, Ca and AlI lines, characteristic of late type stars. Obj 3 was observed by Davies et al. (2012, their number D2-2) and classified as F8/G1, but they concluded that it is in the foreground from its near-infrared colours. We assign G7/8 I spectral type to Obj 21 based on a comparison with the template spectral library of Rayner et al. (2009). Obs. 6, 31, 32, 38 are WR stars previously discovered by Davies et al. (2012, their numbers D2-3, D1-1, D1-5 and D1-2) and Mauerhan et al. (2011, their numbers MDM8 and MDM7). The adopted spectral types are given in Table 2. This method of spectral classification is correct to within 2 subtypes in the near-IR. We adopted this error for our estimates.

3. Results

In this section we describe our methods to determine the fundamental parameters of the young massive clusters, such as the angular size, RV, extinction, distance, age, and mass.

3.1. Angular size

One parameter that can be directly determined is the angular radius of the clusters. We first obtained the coordinates of the cluster centre, based on our stellar catalogue. Starting from a first-guess value, we calculated the radial density profile (RDP) iteratively until we converged towards a best profile. Using this method, we get:

$$\text{Danks 1 : RA(J2000)} = 13:12:26.74$$

$$\text{Dec(J2000)} = -62:41:37.81$$

$$\text{Danks 2 : RA(J2000)} = 13:12:55.14$$

$$\text{Dec(J2000)} = -62:40:52.00$$

$$\text{RCW 79 : RA(J2000)} = 13:40:11.27$$

$$\text{Dec(J2000)} = -61:43:52.10$$

⁷ **IRAF** is distributed by the National Optical Astronomy Observatories (NOAO), which is operated by the Association of Universities for Research in Astronomy, Inc. (AURA) under cooperative agreement with the USA National Science Foundation (NSF).

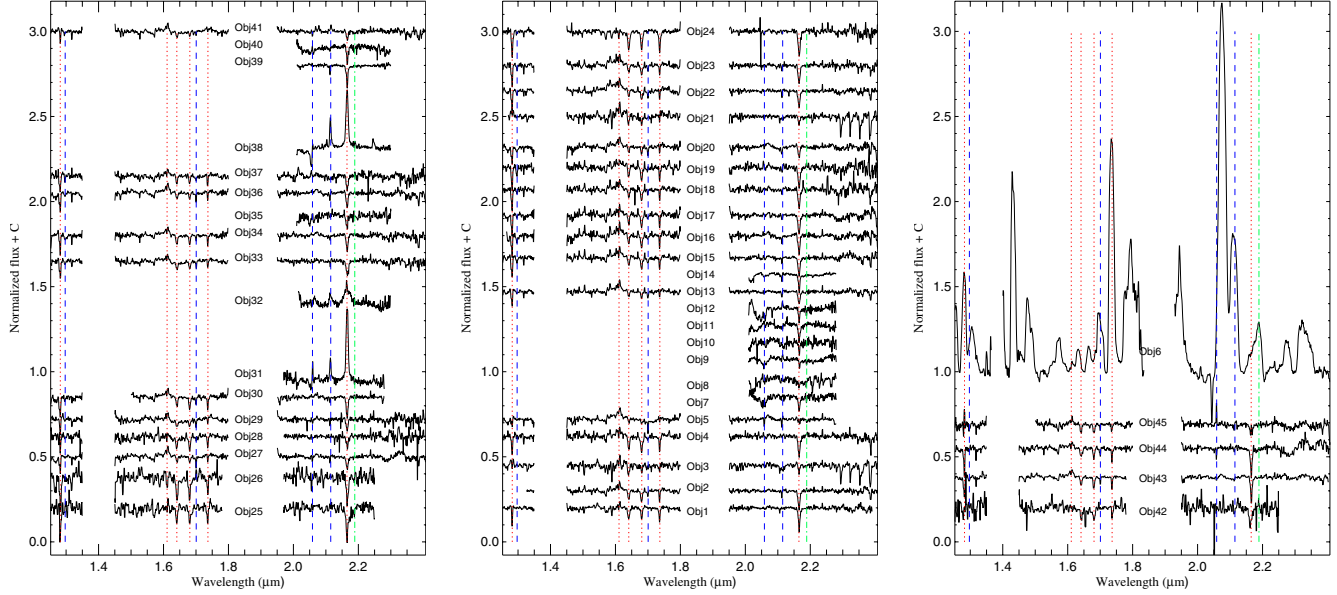


Fig. 4. Spectra of the stars in the area of the clusters Danks 1 (left), Danks 2 (middle) and DBS 132 (right). Obj6 (WC8 type) should be placed with the Danks 2's spectra, but is presented in the right panel for better visibility. Hydrogen recombination lines are marked with vertical dotted, red lines and Helium lines with vertical dashed, blue lines.

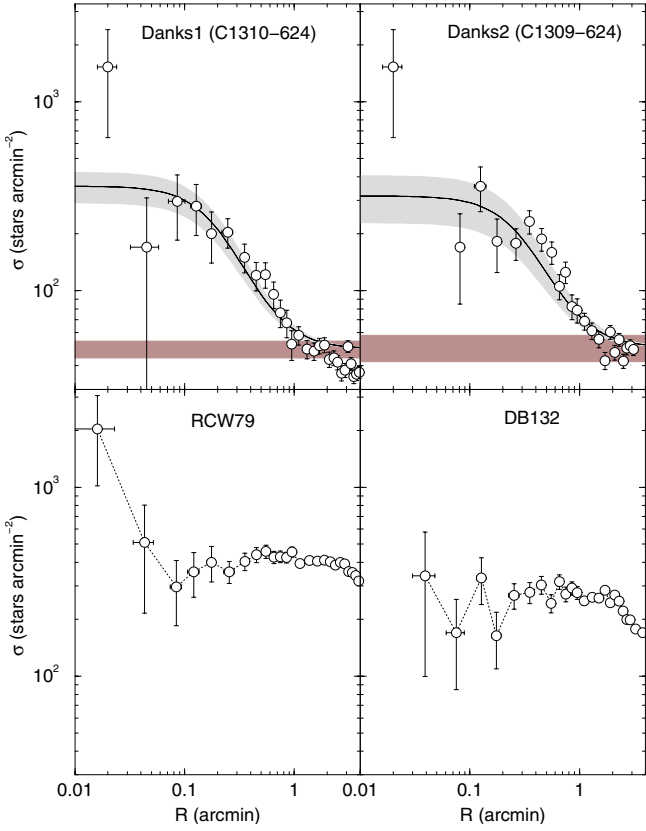


Fig. 5. Radial density profiles for Danks 1, Danks 2 and RCW 79. The error bars are given by Poissonian noise, the solid line shows the fit of a 2-parameter King profile (with uncertainties plotted in grey) and the purple rectangle gives the field density level. Unfortunately, no fit was possible for RCW 79 and DBS 132.

Once the converged RDP is obtained (see results in Fig. 5), we determine the stellar density of the field stars in the vicinity of the clusters. We fit a 2-parameter King profile to each cluster to guide our determination of their angular size. In contrast to

King (1966), we fit the profile to star counts rather than surface brightness. The King profile is defined by 2 parameters, the projected central density of stars (S_0) and the core radius (r_C). The uncertainties on the fit are given by the maximum and minimum values allowed within the error bars of the data points (stemming from Poissonian noise).

We define the angular size of the clusters as the radius where the RDP meets the level of the field stars. An angular size of 1.5 ± 0.5 arcmin is found for both Danks 1 and Danks 2. We also estimate $S_0 = 308 \pm 54$ stars/arcmin 2 and $r_C = 0.21 \pm 0.03$ for Danks 1, and $S_0 = 267 \pm 98$ stars/arcmin 2 and $r_C = 0.32 \pm 0.06$ for Danks 2. RCW 79 does not appear to follow a typical cluster profile. This could be due to artefacts affecting the image, since bright saturated stars leave big holes in the catalogue where the star count is artificially deficient. On the other hand, King profiles are meant to describe relaxed globular clusters, not young open clusters. As such it is not surprising that RCW 79 shows a quite irregular form. Other profiles were also used, but with meaningless results. Still, it shows a stellar density excess at radius $R < 0.1$ arcmin that appears to reach $R \sim 1$ arcmin, hence we can use this value as our estimate of the angular size. As for DB132, the stellar RDP is flat up to $R \sim 3$ arcmin and so is not typical of a cluster.

3.2. Memberships of the spectral targets and RVs

The spectroscopic targets were selected from statistically decontaminated CMDs (Bonatto & Bica 2010). However, as is well known, statistical decontamination methods are unable to perfectly determine cluster membership. As a result, we inevitably obtained some spectra of field stars. Cluster membership could be determined more accurately if proper motions were available. However, at present, the VVV database contains only two years worth of observations and so it is not yet possible to estimate precise proper motions from VVV data.

Therefore, we built the proper motion histograms using the absolute proper motions from the PPMXL Catalogue of Positions and Proper Motions on the ICRS (Roeser et al. 2010). At the distance of Danks 1 and 2 (3–4 kpc, Davies et al. 2012,

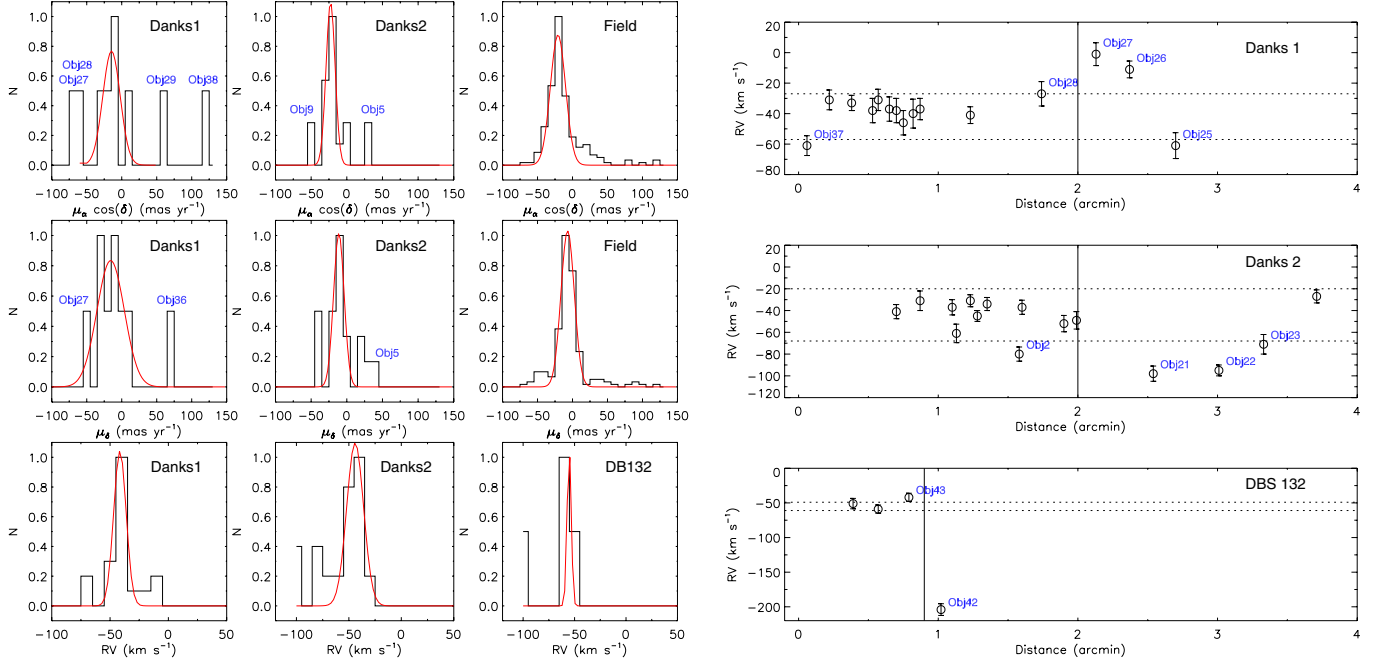


Fig. 6. Left: top and middle panel: histograms and proper motion distributions of $\mu_\alpha \cos \delta$ and μ_δ of Danks 1, Danks 2 and comparison field. Left: bottom panel: RV distributions of Danks 1, Danks 2 and DB132. The solid lines represent the best Gaussian fit, outliers are labelled. Right: radial velocities for our spectroscopic targets as a function of distance from the Danks 1 (top), Danks 2 (middle) and DBS 132 (bottom) cluster centres. The horizontal lines represent the dispersion of the Gaussian fit (see text). The adopted cluster diameter is shown by the vertical line. The error bars represent the random error in determining the RV for each star.

this work) the absolute proper motions are not very accurate (the mean error of the sample is ~ 9 mas), but nevertheless can be used for some estimates (with 40–50% accuracy). Unfortunately, only 9 of the spectroscopic targets in Danks 1 and 18 of Danks 2 appear in the PPXML catalogue. The corresponding proper motion distribution histograms are shown in Fig. 6, together with the proper motion distribution of a comparison field (RA = 198.35231 and Dec = −62.826599). Using the Bonatto & Bica (2011) algorithm, we fitted the distributions with a Gaussian profile, defined by the velocity dispersion (σ) and the average velocity (μ) of the stars (Table 3). Stars outside the 5σ limit of the fit are considered field stars. Such a conservative limit is justified given the large uncertainties on the proper motions.

In addition, the RVs of the spectral targets can also be used to verify cluster membership. We measured the targets' RVs using the IRAF task *rvidlines*, which fits spectral lines to determine the wavelength shift with respect to specified rest wavelengths. In this procedure, we used all H α and HeI lines available in the spectra (typically 7–10 lines per spectrum). We obtained an accuracy equivalent to roughly a tenth of a resolution element, typically ~ 20 km s $^{-1}$. As in the proper motion analysis, we fitted the RV distribution histogram with a Gaussian function. Then, we plotted the RV as a function of distance from the cluster centres (Fig. 6, bottom left and right panels). The dashed lines in Fig. 6 correspond to the 3σ interval, and any star outside those limits is considered a field star. Obs 27 and 28 from Danks 1 can be immediately classified as field stars. Obj 37 (also observed by Davies et al. 2012, their number D1-12) has a peculiar RV, but its spectrum implies cluster membership. The RVs of Danks 2 are much more homogeneous, without obvious outliers. For DBS 132, Obj 42 has a RV that is much higher than the dispersion interval, so it is probably a field star. One should note that this analysis is based on a single epoch observation and follow-up observations of other epochs would be needed to

eliminate bias due to binarity, especially since the binary fraction among OB and WR stars is high ($f_{\text{bin}} > 0.5$ for OB stars; Sana et al. 2011 and references therein; and $f_{\text{bin}} \sim 0.4$ for WR stars; Schnurr et al. 2008 and references therein). The average RVs of each cluster are listed in Table 3. These appear consistent with $v_{\text{LSR}} = -39.4$ km s $^{-1}$ (see Davies et al. 2012, Fig. 7). Additionally, Danks 1 and Danks 2 exhibit the same RV, which indicates that they are binary clusters. The estimated mean RV for DBS 132 is significantly larger than for the Danks clusters, but it is based on only 3 stars. Note that Martins et al. (2010) performed a similar analysis of RCW 79, as such it is not repeated here.

The final check that we performed was to analyse the position of the stars in the $J - K_s$ vs. K_s CMD. Obs 25, 34, 40 and 41 (Danks 1) and Obs 1, 3, 10, 14 and 21 (Danks 2) have peculiar positions in the diagram, far from the MS and the sequence of evolved stars. Of course, this could be due to differential reddening (see discussion in the next section). We attempted to reduce the effect of differential reddening by employing the reddening-free parameter $Q_{\text{IR}} = (J - H) - 1.70(H - K_s)$, as defined by Negueruela et al. (2007) for OB stars (see also Catelan et al. 2011 for a list of several other reddening-free indices in the ZYJHK system). We chose this parameter to avoid the intrinsic degeneracy between reddening and spectral type (and since we expect to find early OB stars in the majority of the clusters in our sample). Figure 7 shows this reddening free parameter vs. K_s magnitude. Originally, Negueruela et al. (2011) defined $Q_{\text{IR}} \leq 0.0 - 0.1$ as a separating value for early-type stars. Subsequently, Ramírez Alegría et al. (2012) and Borissova et al. (2012) defined the separation value for OB stars as $Q_{\text{IR}} \leq 0.3 - 0.4$. Indeed, plotting our objects in the reddening free diagrams, it would appear that Obs 25 and 34 are affected by differential reddening, whilst Obs 40 and 41 show infrared excess and are situated far from the standard OB sequence. Meanwhile, Obs 1, 3, 15, 21 and 24 of Danks 2 occupy peculiar positions on the reddening

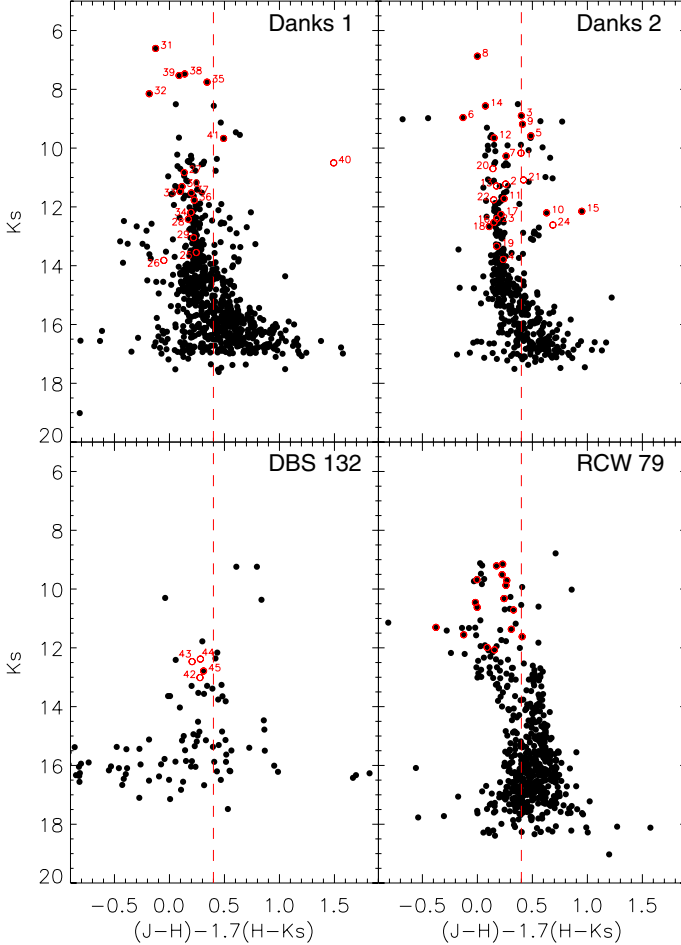


Fig. 7. Reddening free colour of $(J - H) - 1.70(H - K_s)$, also called Q_{IR} plotted vs. K_s magnitude. Red circles mark the stars for which spectra have been observed, and the number attached to them refers to the name of the star listed in Table 2. The red, vertical dashed line is placed at $Q_{\text{IR}} = 0.4$ (see text for more details).

free CMD. Obj 3 was observed and classified by Davies et al. (2012, their number D2-2) as a yellow supergiant (F8-G3 I). It is difficult to determine, with any certainty, if this object is a cluster member. The radial velocity of the object is bigger than the mean value of the cluster (-61 km s^{-1}), but the error is large $\pm 17 \text{ km s}^{-1}$. Its proper motion values are also relatively far from the mean value. Most probably it is a field star, the conclusion Davies et al. (2012) also reach. If not, Danks 2 will be another example of a cluster containing both supergiants and WR stars. However, accurate proper motion measurements are required for its status to be determined. Obs 1, 10, 21 and 24 are most probably field stars. All spectroscopically observed targets in DBS 132 and RCW 79 occupied the region expected of OB stars.

The reddening free CMDs can also be used to separate the MS from the pre-main sequence (PMS) stars. In all cases, except for DBS 132 the PMS population is well separated, and can be defined as stars with $Q_{\text{IR}} > 0.4$ and $K_s > 14$; $K_s > 15$; $K_s > 14$ and $K_s > 13$ mag for Danks 1, Danks 2, DBS 132, and for RCW 79, respectively. This separation was used during isochrone fitting and mass calculation.

3.3. Extinction

The new spectroscopic classifications and infrared observations permit the extinction and reddening law to be evaluated for

the lines-of-sight towards each star studied. The reddening law is known to vary throughout the Galaxy. For example, Turner (2011) noted that dust in the direction of the η Car complex follows an anomalous reddening law. A variable extinction analysis (e.g. Turner 1976; Majaess et al. 2011) may be employed to evaluate both the ratio of total-to-selective-extinction (e.g., $A_{K_s}/E(J - K_s)$) for the line-of-sight and the distance to Danks 1 and Danks 2. Substantial samples are required for the analysis, and thus the clusters were assumed to lie at the same distance. That assumption is supported by the new RVs derived here and the results of Davies et al. (2012). From the expression for computing the distance to a star we get:

$$K_s - M_{K_s} - R_{K_s} \times E(J - K_s) = 5 \times \log d - 5, \quad (1)$$

where we define $R_{K_s} = A_{K_s}/E(J - K_s)$. The equation simplifies for a cluster of stars at a common distance. Rearranging Eq. (1) yields:

$$(K_s - M_{K_s}) = R_{K_s} \times E(J - K_s) + \text{const.} \quad (2)$$

R_{K_s} and $5 \times \log d - 5$ were estimated by comparing $K_s - M_{K_s}$ and $E(J - K_s)$. M_{K_s} and $E(J - K_s)$ were inferred from the new spectroscopic observations by adopting intrinsic parameters from Schmidt-Kaler (1982) and Koornneef (1983). A least squares fit to the data yields $d = 3.6 \pm 0.5 \text{ kpc}$ and $R_{K_s} = 0.60 \pm 0.24$. The results obtained favour the larger distance to Danks 1 and Danks 2 proposed by Davies et al. (2012). This topic is elaborated upon in the next section.

Subsequently, A_{K_s} was estimated for each star, using the value of R_{K_s} derived above. The averages derived from all cluster members are $A_{K_s} = 1.11 \pm 0.24 \text{ mag}$ for Danks 1 and $A_{K_s} = 0.88 \pm 0.34 \text{ mag}$ for Danks 2. The results agree with those determined by Davies et al. (2012), within the uncertainties. For DBS 132 we calculated $A_{K_s} = 1.30 \pm 0.34 \text{ mag}$. We did not obtain spectra of RCW 79's members, but adopting the spectral classification of the stars observed by Martins et al. (2010), we get $A_{K_s} = 0.56 \pm 0.04 \text{ mag}$. The errors represent only the standard deviation from the mean value and can be relatively large in some cases, suggesting differential extinction. In Danks 2, only one star has a particularly large reddening value, namely Obj 14, for which $A_{K_s} = 2.16 \text{ mag}$. Though we note that this star exhibits peculiar behaviour. Excluding it from the calculation we get $A_{K_s} = 0.80 \pm 0.08 \text{ mag}$ for Danks 2. The reddening of DBS 132 is calculated using only 3 spectroscopically observed stars, but the colour spread of DBS 132's cluster CMDs (see below) is $\sim 1 \text{ mag}$. This is much larger than the typical photometric errors, suggesting significant differential extinction. The colour spread is $\sim 0.4 \text{ mag}$ in Danks 1 and $\sim 0.3 \text{ mag}$ in RCW 79, much smaller than in DBS 132, but still significant.

The mean colour-excess inferred for stars in Danks 2 is: $E(J - K_s) = 1.21 \pm 0.02(\sigma_{\bar{x}}) \pm 0.09(\sigma) \text{ mag}$, $E(J - H) = 0.85 \pm 0.02(\sigma_{\bar{x}}) \pm 0.07(\sigma) \text{ mag}$ and $E(B - V) = 2.40 \pm 0.06(\sigma_{\bar{x}}) \pm 0.24(\sigma) \text{ mag}$, where σ is the standard deviation and $\sigma_{\bar{x}}$ is the standard error, i.e. σ divided by the square root of the sample size. The aforementioned mean reddenings were inferred from the intrinsic $BVJH$ colours of Turner (1989) and Straizys & Lazauskaitė (2009), so as to provide an independent check on the extinction estimates determined from the intrinsic parameters of Schmidt-Kaler (1982) and Koornneef (1983) in the preceding paragraph. The mean colour excess inferred from the spectroscopic observations for stars in Danks 1 is: $E(J - K_s) = 1.63 \pm 0.05(\sigma_{\bar{x}}) \pm 0.21(\sigma)$, $E(J - H) = 1.07 \pm 0.04(\sigma_{\bar{x}}) \pm 0.15(\sigma)$ and $E(B - V) = 2.68 \pm 0.06(\sigma_{\bar{x}}) \pm 0.27(\sigma)$. Dust emission observed in WISE images of the field support the finding that Danks 1 suffers additional obscuration relative to Danks 2.

Baume et al. (2009) discovered that the canonical reddening law does not characterize dust associated with the target clusters. The ratio $E(J - H)/E(H - K_s)$ may be inferred from all stars observed along the line of sight. A median (after making a $1.5\sigma_{\bar{x}}$ clip) yields $E(J - H)/E(H - K_s) = 2.20 \pm 0.06(\sigma_{\bar{x}}) \pm 0.37(\sigma)$, which is far in excess of the various values for the inner Galaxy listed in Table 1 of Straižys & Lazauskaitė (2008)'s work. It is also larger than the values tabulated in Majaess et al. (2011) and Majaess et al. (2012). The results imply that the line-of-sight $\ell \sim 305^\circ$ exhibits an anomalous reddening law, thus corroborating the prior findings of Baume et al. (2009). The average JHK_s reddening law for the inner Galaxy is $E(J - H)/E(H - K_s) \sim 2.0$ (Straižys & Lazauskaitė 2009), and Majaess et al. (2011) noted that $E(J - H)/E(H - K_s) \sim 1.94$ appears to describe dust in the field of the classical Cepheid TW Nor. The region encompassing Danks 1 and Danks 2 was not surveyed by Straižys & Lazauskaitė (2009) in their analysis of the reddening law throughout the inner Galaxy. The reddening law determined was subsequently employed to interpret the JHK_s CMDs. An evaluation of the the ratio of total to selective extinction and reddening law in the optical ($E(U - B)/E(B - V)$, R_V) did not yield viable results, presumably since the uncertainties are magnified owing to the added temperature sensitivity of optical passbands and uncertainties tied to acquiring solid U -band photometry (a challenge).

A field star decontaminated $J - H$ vs. $H - K_s$ CCD is presented in Fig. 8. O and B stars are marked with blue and orange circles, respectively. The intrinsic colours of the MS stars and giant branch (Koornneef 1983) are plotted using blue dashed lines. The reddening vector determined above is plotted in orange. Sources located to the right and below the reddening line may have excess emission in the near infrared (IR-excess sources) and/or may be PMS stars.

In this paper we will use $A_{K_s} = 1.11 \pm 0.24$, $A_{K_s} = 0.88 \pm 0.34$ mag, $A_{K_s} = 1.30 \pm 0.34$ mag and $A_{K_s} = 0.56 \pm 0.04$ mag for Danks 1, Danks 2, DBS 132 and RCW 79, respectively. The results are tied to the intrinsic parameters of Schmidt-Kaler (1982) and Koornneef (1983), since R_{K_s} was derived using these studies. Straižys & Lazauskaitė (2009) supply intrinsic colours only. The parameters derived are consistent, within the uncertainties, using either dataset.

3.4. Distances

The distances to the stars for which we have obtained spectra were calculated and are presented in Table 2. The extinction and M_K values determined in the previous section were used to estimate the distance modulus. We then estimated the distance modulus to each cluster by taking the mean of the estimates for its members, using only the members for which we are confident of the spectral type. We get distances of: $(m - M)_0 = 12.7 \pm 0.6$ mag (3.5 ± 1.0 kpc, 8 stars, dwarfs only, namely: Obj 30, 33, 34, 36, 37, 40, 4, D1-10) for Danks 1; $(m - M)_0 = 12.8 \pm 0.5$ mag (3.7 ± 0.5 kpc, 15 stars, dwarfs only, namely: Obj 4, 5, 7, 9, 11, 12, 13, 15, 16, 17, 18, 19, 20, D2-8, D2-7) for Danks 2; $(m - M)_0 = 12.5 \pm 0.2$ mag (3.2 ± 0.3 kpc, 3 stars) for DBS 132. The quoted errors are the standard deviation of the individual stellar distance estimates. Thus we support Davies et al. (2012)'s conclusion that Danks 1 and Danks 2 (and, now, also DBS 132) have the same distance, to within the uncertainties. These distances also corroborate even earlier values obtained by Bica et al. (2004). As for RCW 79, we adopt the spectral classification of the stars observed by Martins et al. (2010) to determine the distance, and get $(m - M)_0 = 13.4 \pm 0.4$ mag (4.8 ± 0.8 kpc).

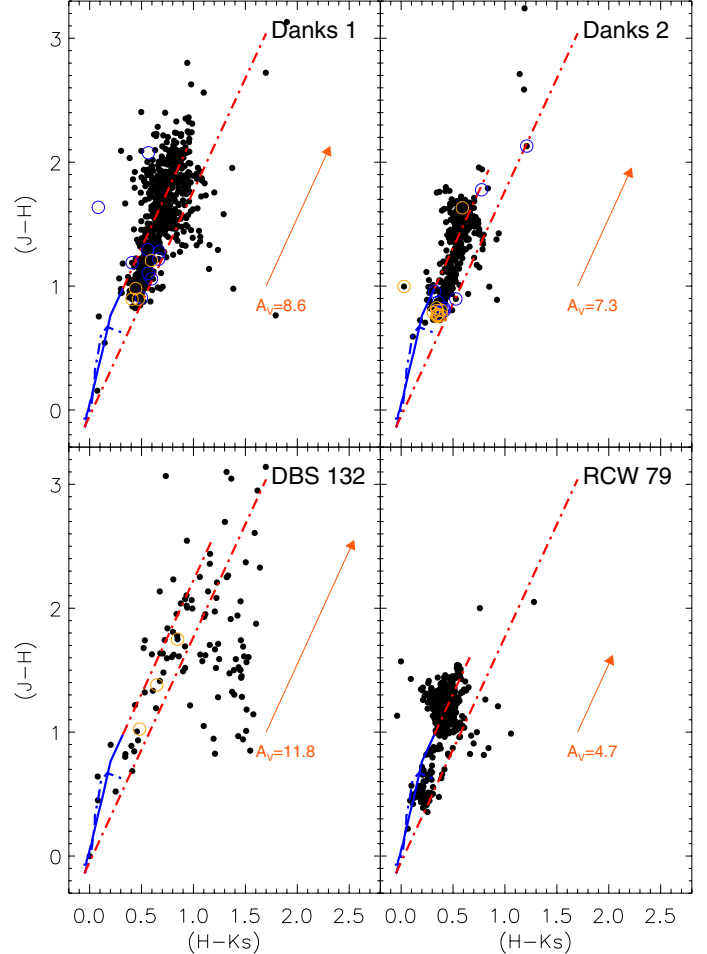


Fig. 8. ($J - H$) vs. ($H - K_s$) colour–colour diagram. The continuous lines represents the sequence of the zero-reddening stars of luminosity class I and class V (Koornneef 1983). The reddening vector is overplotted and the dotted lines are parallel to the standard reddening vector. O and B stars are marked with blue and orange circles, respectively.

3.5. Ages

The ages were estimated by fitting the observed CMDs with solar-metallicity Geneva isochrones (Lejeune & Schaerer 2001) and PMS isochrones (Seiss et al. 2000). Starting with the isochrones set to the previously determined distance modulus and reddening, we apply shifts in magnitude and colour until the fitting statistics reach a minimum value (i.e. difference in magnitude and colour of the stars from the isochrone should be minimal) for both the main sequence and PMS isochrones. We estimate ages of 1–5 Myr for Danks 1, 4–7 Myr for Danks 2, 1–3 Myr for DBS 132 and 2–4 Myr for RCW 79. Figure 9 shows the isochrone fits superimposed on the decontaminated CMDs for all clusters.

However, as can be seen in the Fig. 9, for such young star clusters the main sequence isochrones are almost vertical lines in the near-infrared. Therefore, it is hard to determine the precise age, even using the PMS isochrone set. For this reason and following Liermann et al. (2012), we constructed HR diagrams using only the most luminous stars in Danks 1, Danks 2 and RCW79 (Fig. 10). The effective temperatures for the early-type OB type stars were determined from the spectral types of the stars according to the spectral-type-temperature calibration of Martins et al. (2005). The bolometric corrections are calculated using Eq. (2) of Liermann et al. (2012) and their correction

Table 2. Position, photometry and spectral parameters.

Name	D12 name	RA (J2000)	Dec (J2000)	<i>V</i>	<i>J</i>	<i>H</i>	<i>K_s</i>	RV (km s ⁻¹)	Sp. Typ.	A _K (mag)	<i>d</i> (kpc)
<i>Danks 1 field stars:</i>											
Obj25		13 12 36.310	-62 41 22.60	23.07	15.41	14.15	13.55	-61 ± 17	B9/A0V	1.14 ± 0.05	2.50
Obj26		13 12 35.290	-62 41 53.71	20.49	15.34	14.40	13.82	-11 ± 11	B9/A0V	0.93 ± 0.03	3.11
Obj27		13 12 34.156	-62 41 36.01	18.23	12.08	11.24	10.83	-1 ± 15	B2/3V	0.82 ± 0.04	2.15
Obj28		13 12 32.760	-62 42 07.61	20.43	13.99	12.94	12.42	-27 ± 16	B9/A0V	0.96 ± 0.03	1.61
Obj29		13 12 30.240	-62 41 29.40	20.85	14.46	13.49	13.05	-41 ± 11	B2/3V	0.92 ± 0.04	5.71
Obj40		13 12 23.234	-62 42 01.00	20.23	12.22	10.59	10.50	-37 ± 16	O9/B0V	1.15 ± 0.03	3.56
Obj41	D1-8	13 12 22.879	-62 41 48.83	18.64	11.27	10.08	9.67	-31 ± 14	O4-6	1.08 ± 0.03	4.04
<i>Danks 1 members:</i>											
Obj30		13 12 29.299	-62 42 07.12	21.66	12.67	11.77	11.31	-37 ± 14	B2/3V	0.89 ± 0.06	2.60
Obj31	D1-1	13 12 28.560	-62 41 43.80	14.96	8.26	7.27	6.61	-46 ± 16	WNLh		
Obj32	D1-5	13 12 28.517	-62 41 51.00	16.21	9.81	8.83	8.15	-38 ± 16	WNLh		
Obj33		13 12 28.061	-62 42 08.23	19.29	12.84	11.95	11.48	-31 ± 14	B2/3V	0.89 ± 0.06	2.81
Obj34		13 12 27.459	-62 41 19.27	21.41	13.99	12.78	12.19	-40 ± 19	B2/3V	1.16 ± 0.07	3.45
	D1-7	13 12 26.800	-62 41 56.36	18.16	10.78	8.70	8.14		O4-6 I	1.74 ± 0.03	2.42
	D1-11	13 12 26.320	-62 42 05.78	18.99					O8-B3 V		
	D1-6	13 12 26.220	-62 42 09.37	16.36	9.91	9.01	8.51		O6-8If	0.99 ± 0.04	4.06
Obj35	D1-4	13 12 26.218	-62 41 57.90	16.95	9.61	8.32	7.76		O6-8If	1.26 ± 0.03	2.53
Obj36		13 12 26.107	-62 41 39.89	20.14	13.20	12.22	11.77	-33 ± 10	B2/3V	0.93 ± 0.06	3.16
	D1-9	13 12 26.020	-62 42 15.59	19.01	11.34	10.28	9.69		O4-6	1.11 ± 0.03	4.01
Obj37	D1-12	13 12 25.690	-62 42 05.17	19.39	12.83	11.93	11.53	-61 ± 13	B2/3V	0.86 ± 0.04	2.92
Obj38	D1-2	13 12 25.006	-62 42 00.21	17.40	9.422	8.15	7.48	-31 ± 13	WNLh		
	D1-10	13 12 24.500	-62 42 08.52	19.39	12.10	10.10	10.43		O4-6	1.25 ± 0.03	5.63
Obj39	D1-3	13 12 23.748	-62 42 01.37	17.36	9.41	8.20	7.53	-38 ± 16	O7/8I	1.28 ± 0.03	2.26
<i>Danks 2 field stars:</i>											
Obj1		13 13 11.340	-62 41 10.68	12.25	10.62	10.19	10.17	-41 ± 12	B9/A0V	0.28 ± 0.05	0.78
Obj2		13 13 00.840	-62 39 54.66	17.92	12.32	11.53	11.22	-80 ± 13	B3/4V	0.73 ± 0.06	2.40
Obj3	D2-2	13 12 59.986	-62 40 40.16	12.19	9.61	9.01	8.90	-61 ± 17	F8-G1		
Obj10		13 12 56.112	-62 40 53.90	16.41	14.42	12.79	12.20		B2/3V:	1.41 ± 0.06	3.09
Obj21		13 12 45.300	-62 40 42.16	18.43	12.61	11.50	11.08	-98 ± 14	G7/8I		
Obj22		13 12 43.459	-62 40 57.40	18.22	12.87	12.12	11.76	-95 ± 10	B5/6V	0.72 ± 0.05	2.21
Obj23		13 12 42.250	-62 41 11.42	19.80	13.65	12.79	12.40	-71 ± 18	B5/6V	0.80 ± 0.07	2.85
Obj24		13 12 41.290	-62 41 51.40	20.15	13.72	12.77	12.62	-27 ± 12	B3/4V	0.73 ± 0.07	4.56
<i>Danks 2 members:</i>											
Obj4		13 12 58.930	-62 40 46.49	19.32	15.05	14.17	13.79	-31 ± 18	B8/9V	0.78 ± 0.04	3.81
	D2-7	13 12 58.560	-62 40 54.84	16.73	10.76	9.95	9.56		O4/6V	0.84 ± 0.05	4.75
Obj5	D2-6	13 12 58.351	-62 40 37.34	19.60	10.86	10.04	9.63		O8/9V	0.85 ± 0.04	3.37
Obj6	D2-3	13 12 57.739	-62 40 59.91	17.25	10.83	9.83	8.98		WC7-8		
Obj7		13 12 57.737	-62 40 40.13	17.58	11.50	10.63	10.27		O9/B0V:	0.85 ± 0.03	3.67
	D2-9	13 12 57.083	-62 40 00.49		15.19	13.42	12.64		O6-8		
Obj8	D2-1	13 12 56.419	-62 40 28.43	14.79	8.30	7.40	6.87		O8-B3I	1.00 ± 0.04	1.90
Obj9	D2-4	13 12 56.266	-62 40 51.24	16.41	10.47	9.51	9.19		O6/7 V	0.89 ± 0.05	3.53
Obj11		13 12 54.871	-62 41 03.96	18.73	12.89	12.06	11.72		B2/3V:	0.77 ± 0.06	3.32
Obj12	D2-5	13 12 54.485	-62 41 05.01	16.62	10.80	10.02	9.65		O7/8V	0.81 ± 0.03	4.09
	D2-8	13 12 54.370	-62 40 45.48	16.80	11.14	10.34	9.92		O6-8V	0.84 ± 0.05	3.87
Obj13		13 12 52.730	-62 40 54.51	17.93	12.41	11.64	11.29	-41 ± 13	B0/1V	0.77 ± 0.07	4.91
Obj14		13 12 51.773	-62 39 55.96	18.75	11.91	9.78	8.57	-31 ± 11	O7/8I	2.16 ± 0.03	2.43
Obj15		13 12 51.221	-62 41 02.38	19.43	13.17	12.18	12.15	-37 ± 14	B3/4V	0.68 ± 0.06	3.76
Obj16		13 12 50.541	-62 40 22.86	19.54	13.72	12.91	12.53	-45 ± 10	B5/6V	0.76 ± 0.07	3.08
Obj17		13 12 50.160	-62 41 00.96	18.85	13.41	12.60	12.26	-34 ± 12	B5/6V	0.74 ± 0.07	2.75
Obj18		13 12 49.159	-62 41 00.20	19.39	13.82	13.05	12.67	-37 ± 13	B5/6V	0.74 ± 0.07	3.32
Obj19		13 12 48.130	-62 41 13.36	19.88	14.44	13.68	13.34	-52 ± 15	B7/8V	0.69 ± 0.13	3.71
Obj20		13 12 47.520	-62 40 54.48	17.40	11.82	11.06	10.60	-49 ± 16	B0/1V	0.77 ± 0.07	3.74
<i>DBS2003 132 field star:</i>											
Obj42		13 12 22.270	-62 42 38.28	22.05	14.70	13.53	13.01	-204 ± 17	B7/8V	1.04 ± 0.13	2.49
<i>DBS2003 132 members:</i>											
Obj43		13 12 21.004	-62 41 48.41	20.78	13.98	12.95	12.47	-42 ± 12	B5/6V	0.96 ± 0.07	2.87
Obj44		13 12 19.871	-62 42 25.23	23.02	14.41	13.03	12.38	-51 ± 15	B3/4V	1.30 ± 0.06	3.35
Obj45		13 12 16.202	-62 42 10.20	21.06	15.39	13.64	12.79	-59 ± 12	B3/4V	1.64 ± 0.06	3.44

Notes. Columns include the name of the star, the Davies et al. (2012, hereafter D12) identification number, the right ascension (RA), the declination (Dec), *V* (taken from Baume et al. 2009), *J*, *H* and *K_s* photometry (in mag), the RV, the spectral type (determine from comparison with template spectra and *UBV* photometry), extinction (A_K) and distance (*d*), respectively. Stars are ordered as a function of their (non-)membership.

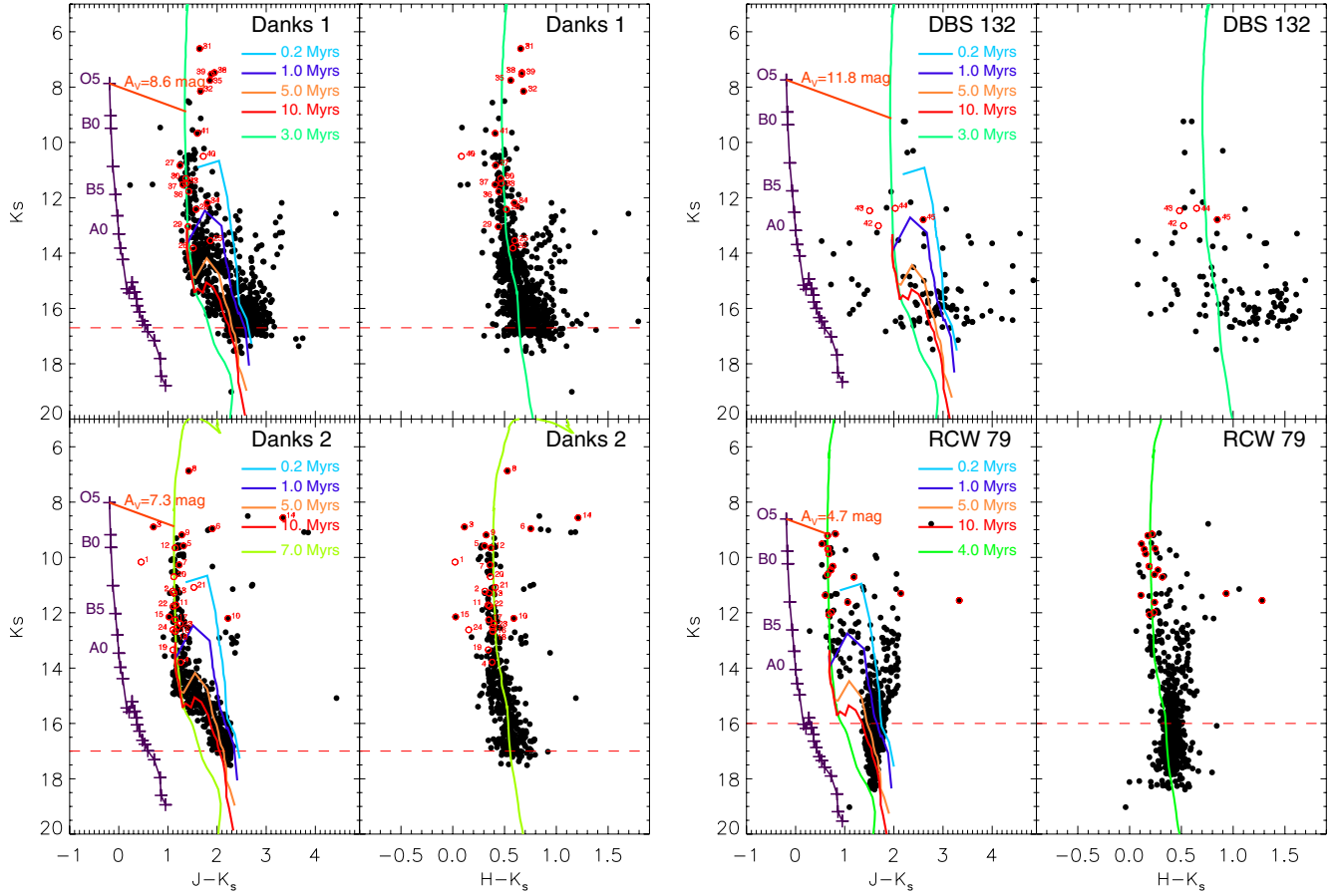


Fig. 9. The colour–magnitude diagrams for the four studied clusters. The Schmidt-Kaler (1982) sequence is shown in the $(J - K_s)$ vs. K_s diagram. Red circles mark the stars for which spectra have been observed, and the number attached to them refers to the name of the star listed in Table 2. The red dashed lines represent 50% completeness limit. The green line is the main-sequence model (the exact colour changes with the age used), whereas the others (light blue, dark blue, orange and read) are PMS models. See text for more details.

Table 3. Proper motion and RV components.

Name	N stars	Mean ($\mu_\alpha \cos \delta$) mas yr $^{-1}$	$\sigma_{\mu_\alpha \cos \delta}$ mas yr $^{-1}$	Mean (μ_δ) mas yr $^{-1}$	σ_{μ_δ} mas yr $^{-1}$	Mean (RV) km s $^{-1}$	σ_{RV} km s $^{-1}$
Field	194	-21 ± 1	11 ± 1	-7 ± 1	10 ± 1	--	–
Danks 1	9	-28 ± 2	12 ± 3	-16 ± 4	19 ± 4	-42 ± 1	5.0 ± 0.5
Danks 2	18	-23 ± 1	6 ± 1	-11 ± 1	7 ± 1	-44 ± 1	8.0 ± 1.0
DB132	5	–	–	–	–	-55 ± 5	2.0 ± 1.0

Table 4. Physical parameters of the clusters.

Cluster	Slope	Mass (PMS) M_\odot	Mass (MS) M_\odot	Total Mass M_\odot
Danks 1	-1.43 ± 0.17	900^{+50}_{-30}	7000^{+1450}_{-1000}	7900^{+1400}_{-1050}
Danks 2	-1.23 ± 0.22	600^{+50}_{-50}	2300^{+800}_{-500}	2900^{+850}_{-550}
RCW 79	-1.05 ± 0.28	500^{+200}_{-100}	2500^{+750}_{-300}	3000^{+950}_{-450}
DB 132	-0.97 ± 0.39	>60	>265	>345

to BC_K . The bolometric corrections for WR stars are taken from Martins et al. (2008). Absolute stellar magnitudes were derived from the K_s magnitudes given in Table 2, with extinction and distance derived from their spectral types.

We then compared the distribution of the stars with the latest isochrones and stellar tracks (with rotation) taken from Ekström et al. (2012). The temperatures and luminosities of stars in

RCW79 were taken directly from Martins et al. (2010). Here we repeated their Fig. 7, though now the same isochrones and stellar tracks system as with the other clusters. As can be seen, most of the stars are concentrated around 3, 5 and 4 Myr isochrones for Danks 1, Danks 2 and RCW79 respectively. In comparison to the Davies et al. (2012) age determination, we derived slightly older ages for Danks 1 and Danks 2. However, taking in to account the large uncertainties on the determined ages, we consider our results in good agreement. Martins et al. (2010) also derived a younger age for RCW 79 (2.3 ± 0.5 Myr), but again, this is consistent with our determination.

3.6. Initial mass function and cluster masses

By looking at the clusters’ CMDs it was often obvious which stars were not genuine cluster members or were not MS objects. Some of these spurious objects are by-products of our de-contamination method (see Sect. 2.1.2). There were also some

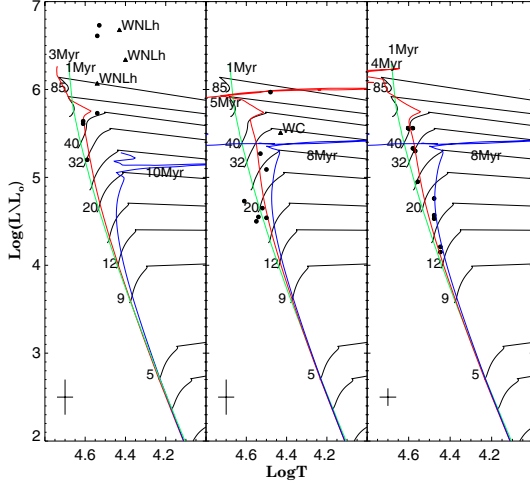


Fig. 10. Hertzsprung-Russell diagrams for the Danks 1, Danks 2 and RCW79. Circles represent the early-type O stars, triangles the WR stars. The isochrones and stellar evolutionary tracks are from Ekström et al. (2012).

Wolf-Rayet stars that needed to be removed. The LF was converted to the Initial Mass Function (IMF) using the Geneva isochrones, assuming solar metallicity and ages of 3, 5, 4 and 2 Myrs for Danks 1, Danks 2, RCW 79 and DBS 132 respectively. For each cluster we established the MS turn-on point and assumed everything fainter than this to be PMS. This point was found to be at $K_s \sim 14$ for Danks 1, Danks 2 and DB 132, and $K_s \sim 13$ for RCW79.

Our calculated slopes of $\Gamma = -1.43 \pm 0.17$ for Danks 1 and $\Gamma = -1.23 \pm 0.22$ for Danks 2, are consistent with the Salpeter slope ($\Gamma = -1.35$), to within 1σ , as well as with Davies et al. (2012) results. These slopes were used to extrapolate the masses of the observed MS stars to provide a total mass for the cluster. For extrapolation of masses below $<0.5 M_\odot$ we used the Kroupa value of $\Gamma = -0.3$. This gave a total mass of $7900^{+1400}_{-1050} M_\odot$ for Danks 1 and $2900^{+850}_{-550} M_\odot$ for Danks 2. The results are in very good agreement with those found in Davies et al. (2012): $8000 \pm 1500 M_\odot$ for Danks 1 and $3000 \pm 800 M_\odot$ Danks 2.

RCW 79 has a slope of $\Gamma = -1.05 \pm 0.28$, with a mass of $3000^{+950}_{-450} M_\odot$. DB 132 did not contain enough stars to reliably estimate a slope, nor completeness for each magnitude band. However, using the same methodology as demonstrated above, we suggest a minimum mass of $\sim 400 M_\odot$.

It should be noted that the stellar mass function is not the same as the IMF, despite the young age of the clusters. Dynamical evolution of the cluster will result in the loss of stars through the equipartition of energy, leading to a higher average star-mass and an increase in the binarity proportion. This will affect the slope of the stellar mass function, flattening it. This process is dependant on both cluster mass and lifetime, particularly for those with $<10^4 M_\odot$ and life-times of a few 100 Myr (Kroupa et al. 2011). Therefore, the clusters' dynamical evolution must be considered.

4. Search for variable stars

The VVV survey provides many epochs of observations in the K_s -band. So far, now that the second year of the survey is completed, a small fraction of the total number of expected epochs have been obtained in the Galactic disk. This could be enough to look for variable candidates and perhaps obtain some

periodicities. An observation log of the K_s observations of the two VVV fields which contain the clusters studied in this paper is presented in Table 1.

Amongst the VVV-SkZ_pipeline's outputs is a table of calibrated magnitudes of individual K_s -band frames. Unfortunately, not all observations were obtained in the weather conditions required for the VVV survey and about half of them had to be rejected. To verify our method for calibrating the K_s -band photometry in each individual frame, we verified that all frames share the same magnitude zero-point value by subtracting the magnitude of all observed stars with $12.5 \text{ mag} < K_s < 14.5 \text{ mag}$. For all frames, we get offsets close to 0, with an error comparable to the photometric accuracy. Figure 11 shows the standard deviation, σ_{K_s} , as a function of the mean value, K_s , of the extracted light curves. A greyscale plot is used for better visibility. A theoretical relationship between K_s and the photometric accuracy can be obtained starting with the definition of magnitude:

$$K_s = -2.5 \log FI + R + m_0, \quad (3)$$

where F is the mean value of the flat-field, R , the mean value of the readout, m_0 , the magnitude zero-point and I is the integrated observed total flux of a given star. Using the propagation of error formula, we obtain:

$$\sigma_{K_s} = \frac{2.5 \log e}{I} \sqrt{(\sigma_F I)^2 + I + \sigma_R^2}, \quad (4)$$

where σ_F is the error on the flat-field (here, assumed to be 1%) and $\sigma_R = [\sqrt{\pi}(\text{size of the seeing}) \times (\text{readnoise per pixel})]$ is the error on the readout. The only value that needs to be fitted to the data is m_0 , and values of 23.8 mag and 23.5 mag were found for d084 and d086. This function is overplotted on the data in Fig. 11 with a solid green line.

Due to saturation effects, the observed values of σ_{K_s} deviate from Eq. (4) when K_s is brighter than ~ 12.5 mag. Hence, for these magnitudes, we instead use a logarithmic function derived from fitting a slope to the $\log \sigma_{K_s}$ relation. Using this relation, one could determine a first list of candidate variables, setting a threshold at $5 \times \sigma_{K_s}$. Stars meeting this criteria are marked with filled red circles in Fig. 11.

However, in addition to the intrinsic variability of stars, σ_{K_s} contains systematic uncertainties that vary, depending on the position of the star on the detector (due to varying read noise and/or flat-field properties and/or presence of varying local background due to a nearby bright/saturated star). Hence, we adopt the approach described in Dékány et al. (2011). During each acquisition of VVV data for fields d084 and d086, we systematically obtain for each epoch two frames within a few minutes. This allows us to get the internal scatter of the time-series, σ_i , defined as:

$$\sigma_i = \sum_{j=1}^{N-1} (m_j - m_{j+1})^2 / 2M, \quad (5)$$

where m_j is the magnitude of the j th detection. The sum is evaluated for M pairs of detections, each obtained within less than 5 min of each other. Candidate variable stars with $\sigma_{K_s}/\sigma_i \geq 2.5$ are shown as blue dots in Fig. 11.

Unfortunately, due to bad weather, light curves rarely have more than 15 data points of an appropriate accuracy. Therefore, periodograms are very noisy and do not show any clear signal. On the other hand, some long term and/or high amplitude variations can be identified. We add to the Online Material a list of variable candidates contained in the four clusters, along with a

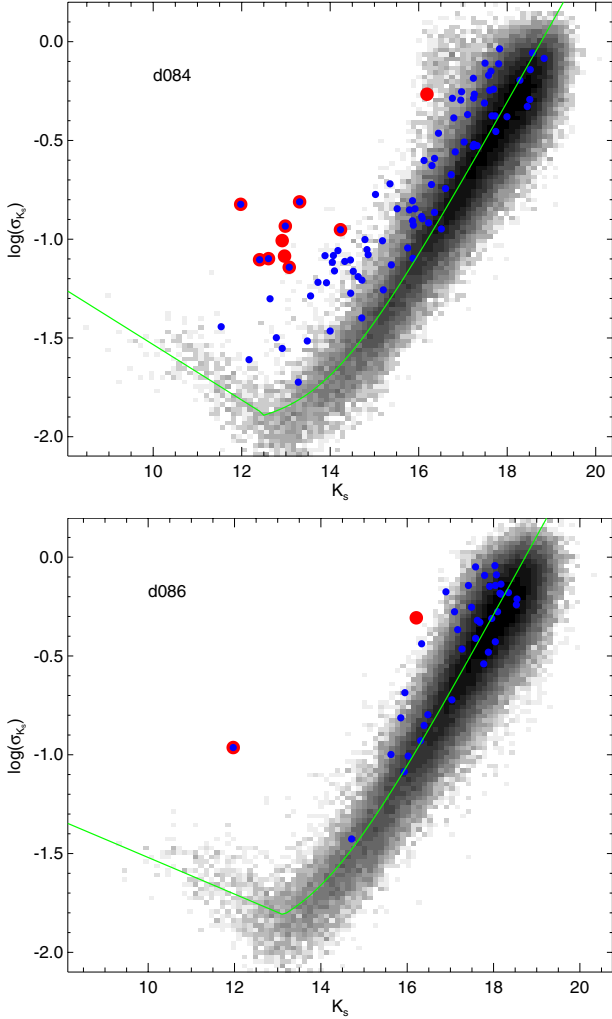


Fig. 11. Standard deviation (σ_{K_s}) of the K_s -band light-curve extracted from the VVV fields d084 and d086. The fit of a theoretical relation between the K_s and the photometric accuracy is plotted in solid, green line. The variable candidates among the stars in the radius of the four studied clusters are shown. Big, red circles are stars having a variability amplitude higher than $5\sigma_{K_s}$, while small, blue circles are stars with $\sigma_i/\sigma_{K_s} \geq 2.5$, where σ_i is the internal scatter of the time-series.

brief description of their variations. Also, for both VVV regions studied, i.e. d084 and d086, we find a fraction of 1.5% and 2% of variable sources, respectively, which is in a agreement with the results of Dékany et al. (2011) and Pietrukowicz et al. (2011).

5. Discussion

5.1. The G305 star forming complex

This study provides additional information about the G305 star forming complex. In addition to the diffuse population of massive stars mentioned in Davies et al. (2012; see also Shara et al. 2009; and Mauerhan et al. 2011), our spectral observations reveal 12 early B stars with distances that are comparable with Danks 1 and Danks 2. Therefore, although not cluster members they are definitely members of the G305 star forming complex. At this stage, it is hard to confirm if they are or are not runaway stars, because we cannot yet measure the proper motions using VVV data. Alternatively, they could be part of a larger association of young stars surrounding Danks 1 and 2, formed within the same molecular cloud.

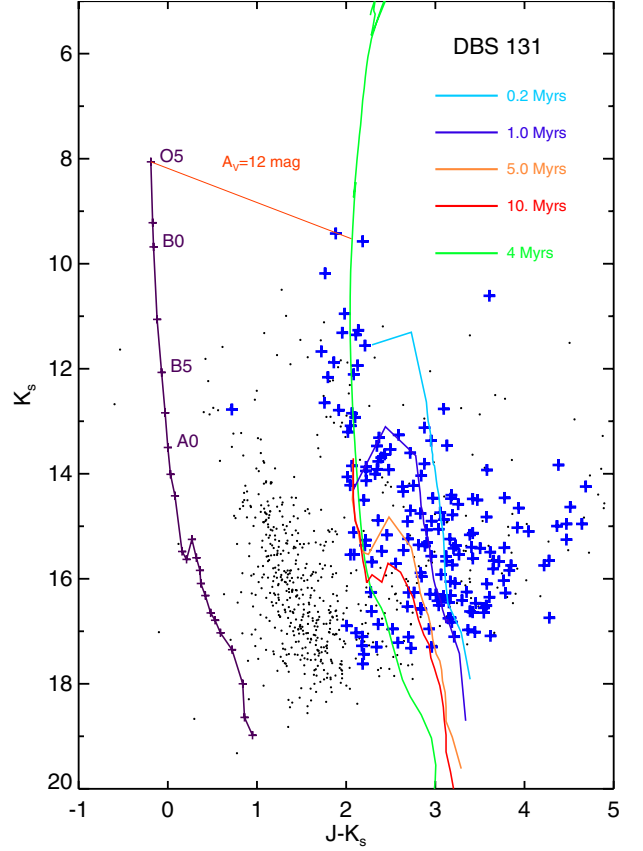


Fig. 12. ($J - K_s$) vs. K_s diagram for DBS 131, presented as in Fig. 9. Dark dots are field stars and blue crosses are cluster stars.

Taking advantage of the VVV wide field of view, we examined the stellar content of the regions outlined by Hindson et al. (2010). There are a number of already catalogued clusters in this region, namely: Danks 1, Danks 2, DBS 83, DBS 84, DBS 130, DBS 131 (IR cluster G305.24+0.204, Clark et al. 2004; Leistra et al. 2005; Longmore et al. 2007), DBS 132, DBS 133, DBS 134, and G305.363+0.179 (Clark et al. 2004). In addition to these, we have found three new young star clusters and/or stellar groups: VVV CL023, VVV CL022, VVV CL021 (Borissova et al. 2011), and a new star forming region SFR1. The preliminary VVV CMD of G305.24+0.204 (DBS 131) is shown in Fig. 12, where, in addition to a well defined MS, highlighted previously by Leistra et al. (2005) and Longmore et al. (2007), the PMS population is readily apparent in the VVV data. The adopted parameters of the plot are $m - M = 12.85$ mag (3.72 kpc), $E(J - K) = 2.25$ mag, age 3–5 Myr. DBS 131, like all other clusters from the G305 complex listed here, is very young (less than 5 Myr) and less massive than Danks 1 and Danks 2. A more detailed analysis of these objects will be presented in the next paper in our series (Borissova et al., in prep.).

5.2. Milky Way's structure

The clusters' context within the Milky Way's structure is now assessed. The depth of the VVV photometry permits the mapping of crowded low latitude Galactic fields (Minniti et al. 2011). The youth of the stellar constituents inferred from the spectral types (Table 2) implies that Danks 1 and Danks 2 are viable tracers of the Galaxy's spiral structure. Georgelin et al. (1988) first mentioned that the G305 region should be within the Scutum-Crux arm of the Galaxy. Later, Baume et al. (2009) noted that Danks 1

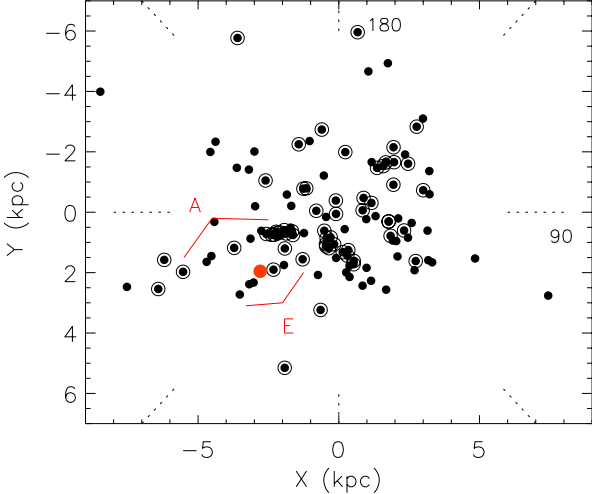


Fig. 13. Map of local spiral structure as delineated by long period classical Cepheids (dots) and young clusters (circled dots) (see also Majaess et al. 2009). The Carina (A) and Centaurus (E) spiral arms are indicated on the diagram. Danks 1 and Danks 2 (red dot) reside in the Centaurus spiral arm.

and Danks 2 may belong to the Carina spiral arm. That conclusion is tied to their distance, which is significantly nearer ($>50\%$) than that found here. Their optical distance is acutely sensitive to variations in R_V , particularly since the total extinction in the optical $A_V = R_V \times E(B-V)$ is sizeable, and not constrained by any spectroscopic observation. The present results support the larger distance cited by Davies et al. (2012).

The positions of Danks 1 and Danks 2 are plotted, in Fig. 13, on a hybrid map of the Galaxy's spiral structure, as delineated by long-period classical Cepheids and young (<10 Myr) open clusters. Long-period Cepheids are more massive younger stars than their shorter period counterparts, since the variables follow a period-luminosity relation. Cepheid variables and young open clusters define an analogous (local) spiral pattern (e.g. Majaess et al. 2009). Danks 1 and Danks 2 lie beyond the Sagittarius-Carina spiral arm and occupy the Centaurus arm, along with numerous young Cepheids and clusters (e.g., TW Nor, VW Cen, and VVV CL070). VVV CL070 was discovered in the comprehensive survey by Borissova et al. (2011), who discovered 96 new clusters in the region sampled by the VVV survey.

6. Summary

In this paper we study three young known massive star clusters using data from the VVV survey and complementary low-resolution near-IR spectroscopy. Two of these clusters, Danks 1 and Danks 2, were investigated by Davies et al. (2012), whilst Martins et al. (2010) provide excellent spectroscopic observations of the brightest members of RCW 79. We choose these clusters to test and describe our methodology, which we will employ to study hundreds of open clusters observed by the VVV survey.

The new analysis of Danks 1 and Danks 2 can be compared with that of Davies et al. (2012). We obtain comparable values of reddening, however, our results are based on many more spectra and use VVV JHK_s CMDs and CCDs. Our results account for differential reddening and the reddening laws were established for the line of sight, thus preventing uncertainties from propagating into the distance determination. Secondly, we also obtain similar distances. But, while their analysis was limited by the uncertainty on the luminosity class assignment, since they

mostly observed bright stars that are near the turnoff, ours is less affected, as we have access to spectra of many B dwarf stars. The agreement with Davies et al. (2012)'s results also calls into question the much smaller distances determined by Baume et al. (2009).

We derive comparable cluster masses to those estimated by Davies et al. (2012). We also estimate that Danks 1 and Danks 2 are 3 and 5 Myr old respectively. Therefore, slightly older than Davies et al. (2012) suggest, but consistent within the uncertainties. Taking advantage of the large field of view of VVV, we report a significant population of pre-main sequence stars. Interestingly enough, Danks 2 contains the highest fraction (16% of the total mass) of PMS stars, followed by RCW 79 (15%) and Danks 1 (only 4%). Based on radial velocity analysis, we found that Danks 1 and Danks 2 have the same mean radial velocity, which indicates that they are indeed binary clusters. A list of candidate variable stars is presented, which we will confirm as we obtain more VVV images.

We also report our results for DBS 132 and DBS 131, open clusters situated near the two Danks clusters. Both clusters are very young (1–3 Myr), still embedded in dust and gas, and less massive than the Danks clusters. In addition to the diffuse population of massive WR stars, our spectral observations reveal 12 early B stars with distances that are comparable with Danks 1 and Danks 2. Therefore, although not cluster members they are members of the G305 star forming complex. The G305 complex most probably lies in the Centaurus arm, beyond the Sagittarius-Carina spiral arm. Finally, we present the first deep infrared colour-magnitude diagram of RCW79, revealing a large pre-main sequence population. We calculated the mass of this cluster to be roughly $3000 M_\odot$.

Acknowledgements. We would like to warmly acknowledge J. P. Emerson for very fruitful discussions. This project is supported by the Chilean Ministry for the Economy, Development, and Tourism's Programa Iniciativa Científica Milenio through grant P07-021-F, awarded to The Milky Way Millennium Nucleus. ANC gratefully acknowledges support from the Chilean Centro de Astrofísica FONDAP No. 15010003 and the Chilean Centro de Excelencia en Astrofísica y Tecnologías Afines (CATA) and Comité Mixto ESO-GOBIERNO DE CHILE. J.B. is supported by FONDECYT No. 1120601 and by the Ministry for the Economy, Development, and Tourism's Programa Iniciativa Científica Milenio through grant P07-021-F, awarded to The Milky Way Millennium Nucleus. J.R.A.C. is also supported by FONDECYT Regular #1080086. R.K. is supported by Centro de Astrofísica de Valparaíso and Proyecto DIUV23/2009. D.G. also acknowledges FONDAP and CATA funds. D.M. is supported by FONDECYT Regular #1090213, by the FONDAP Center for Astrophysics #15010003, by the BASAL CATA Center for Astrophysics and Associated Technologies PFB-06, and by the MILENIO Milky Way Millennium Nucleus from the Ministry of Economy's ICM grant P07-021-F. R.d.G. acknowledges partial research support through grant 11073001 from the National Natural Science Foundation of China. M.S.N.K. is supported by a Ciência 2007 contract, funded by FCT/MCTES (Portugal) and POPH/FSE (EC). The data used in this paper have been obtained with NTT/SofI at the ESO La Silla Observatory, and with Clay/MMIRS at Las Campanas Observatory. This research has made use of the SIMBAD database, operated at CDS, Strasbourg, France. We gratefully acknowledge use of data from the ESO Public Survey programme ID 179.B-2002 taken with the VISTA telescope, and data products from the Cambridge Astronomical Survey Unit.

References

- Baume, G., Carraro, G., & Momany, Y. 2009, MNRAS, 398, 221
- Bessell, M. S., Castelli, F., & Plez, B. 1998, A&A, 333, 231
- Bica, E., Ortolani, S., Momany, Y., Dutra, C. M., & Barbuy, B. 2004, MNRAS, 352, 226
- Bik, A., Kaper, L., Hanson, M. M., & Smits, M. 2005, A&A, 440, 121
- Bonatto, C., & Bica, E. 2010, A&A, 516, A81
- Bonatto, C., & Bica, E. 2011, MNRAS, 415, 313
- Borissova, J., Bonatto, C., Kurtev, R., et al. 2011, A&A, 532, A131
- Borissova, J., Georgiev, L., Hanson, M. M., et al. 2012, A&A, submitted
- Cardelli, J. A., Clayton, G. C., & Mathis, J. S. 1989, ApJ, 345, 245

- Catelan, M., Minniti, D., Lucas, P. W., et al. 2011, in Carnegie Observatories Astrophysics Series, RR Lyrae Stars, Metal-Poor Stars, and the Galaxy, ed. A. McWilliam, 5, 145
- Clark, J. S., & Porter, J. M. 2004, A&A, 427, 839
- Crowther, P., Hadfield, L., Clark, J. S., Negueruela, I., & Vacca, W. 2006, MNRAS, 372, 1407
- Danks, A. C., Dennefeld, M., Wamsteker, W., & Shaver, P. A. 1983, A&A, 118, 301
- Davies, B., Clark, J. S., Trombley, C., et al. 2012, MNRAS, 419, 1871
- Dekany, I., Catelan, M., Minniti, D., & the VVV Collaboration 2011 [arXiv:1111.0909v2]
- Dias, W. S., Alessi, B. S., Moitinho, A., & Lépine, J. R. D. 2002, A&A, 389, 871
- Dutra, C. M., Santiago, B. X., & Bica, E. 2002, A&A, 383, 219
- Elmegreen, B. G. 2007, ApJ, 668, 1064
- Emerson, J. P., & Sutherland, W. 2010, The Messenger, 139, 2
- Ekström, S., Georgy, C., Eggenberger, P., et al. 2012, A&A, 537, A146
- Figer, D. F., McLean, I. S., & Najarro, F. 1997, ApJ, 486, 420
- Fischera, J., & Dopita, M. A. 2004, ApJ, 611, 919
- Gehrels, N. 1986, ApJ, 303, 336
- Georgelin, Y. M., Boulesteix, J., Georgelin, Y. P., Le Coarer, E., & Marcellin, M. 1988, A&A, 205, 95
- Girardi, L., Williams, B., Gilbert, K., Rosenfield, P., & Dalcanton, J. 2010, ApJ, 724, 1030
- Hanson, M. M., Conti, P. S., & Rieke, M. J. 1996, ApJS, 107, 281
- Hanson, M. M., Rieke, M. J., & Luhman, K. L. 1998, AJ, 116, 1915
- Hanson, M. M., Kudritzki, R.-P., Kenworthy, M. A., Puls, J., & Tokunaga, A. T. 2005, ApJS, 161, 154
- Hanson, M. M., Kurtev, R., Borissova, J., et al. 2010 A&A, 516, A35
- Hillier, D. J., & Miller, D. L. 1998, ApJ, 496, 407
- Hindson, L., Thompson, M. A., Urquhart, J. S., Clark, J. S., & Davies, B. 2010, MNRAS, 408, 1438
- Irwin, M. J., Lewis, J., Hodgkin, S., et al. 2004, in SPIE Conf. Ser. 5493, eds. P. J. Quinn, & A. Bridger, 411
- Ivanov, V. D., Kurtev, R., & Borissova, J. 2005, A&A, 442, 195
- Koornneef, J. 1983, A&A, 128, 84
- King, I. R. 1966, AJ, 71, 64
- Kroupa, P., Weidner, C., Pflamm-Altenburg, J., et al. 2011 [arXiv:1112.3340]
- Lada, C. J., & Lada, E. A. 2003, ARA&A, 41, 57
- Lejeune, T., & Schaerer, D. 2001, A&A, 366, 538
- Leistra, A., Cotera, A. S., Liebert, J., & Burton, M. 2005, AJ, 130, 1719
- Liermann, A., Hamann, W.-R., & Oskinova, L. M. 2009, A&A, 494, 1137
- Liermann, A., Hamann, W.-R., & Oskinova, L. M. 2012, A&A, 540, A14
- Livingston, W., & Wallace, L. 1991, National Solar Observatory: “An atlas of the solar spectrum in the infrared from 1850 to 9000 cm⁻¹”, Technical Report #91-001
- Longmore, S. N., Maercker, M., Ramstedt, S., & Burton, M. G. 2007, MNRAS, 380, 1497
- Longmore, A. J., Kurtev, R., Lucas, P. W., et al. M. 2011, MNRAS, 416, 465
- Maiolino, R., Rieke, G. H., & Rieke, M. J. 1996, AJ, 111, 537
- Majaess, D. J., Turner, D. G., & Lane, D. J. 2009, MNRAS, 398, 263
- Majaess, D. J., Turner, D., Moni Bidin, C., et al. 2011, ApJ, 741, L27
- Majaess, D. J., Turner, D., Moni Bidin, C., et al. 2012, A&A, 537, L4
- Martins, F., Genzel, R., Hillier, D. J., et al. 2007, A&A, 468, 233
- Martins, F., Schaefer, D., & Hillier, D. J. 2005, A&A, 436, 1049
- Martins, F., Hillier, D. J., Paumard, T., et al. 2008, A&A, 478, 219
- Martins, F., Pomarès, M., Deharveng, L., Zavagno, A., & Bouret, J.-C. 2010, A&A, 510, A32
- Mauerhan, J., Van Dyk, S., & Morris, P. 2011, AJ, 142, 40
- Mauro, F., Moni Bidin, C., Chené, A.-N., et al. 2012, PASP, submitted
- Monnier, J. D., Tuthill, P. G., Danchi, W. C., Murphy, N., & Harries, T. J. 2007, ApJ, 655, 1033
- Minniti, D., Lucas, P. W., Emerson, J. P., et al. 2010, New A, 15, 433
- Minniti, D., Saito, R., Alonso-García, J., Lucas, P. W., & Hempel, M. 2011, ApJ, 733, L43
- Morris, P. W., Eenens, P. R. J., Hanson, M. M., Conti, P. S., & Blum, R. D. 1996, ApJ, 470, 597
- Moorwood, A., Cuby, J.-G., & Lidman, C. 1998, The Messenger, 91, 9
- Negueruela, I., Marco, A., Israel, G. L., & Bernabeu, G. 2007, A&A, 471, 485
- Negueruela, I., González-Fernández, C., Marco, A., & Clark, J. S. 2011, A&A, 528, A59
- Roeser, S., Demleitner, M., & Schilbach, E. 2010, AJ, 139, 2440
- Pietrukowicz, P., Minniti, D., Alonso-García, J., & Hempel, M. 2012, A&A, 537, A116
- Portegies Zwart, S. F., McMillan, S. L. W., & Gieles, M. 2010, ARA&A, 48, 431
- Price, D. J., Bate, M. R. 2009, MNRAS, 398, 33
- Ramírez Alegría, S., Marín-Franch, A., & Herrero, A. 2012, A&A, 541, A75
- Rayner, J. T., Cushing, M. C., & Vacca, W. D. 2009, ApJS, 185, 289
- Rieke, G. H., & Lebofsky, M. J. 1985, ApJ, 288, 618
- Sana, H., James, G., & Gosset, E. 2011, MNRAS, 416, 817
- Saito, R. K., Hempel, M., Minniti, D., et al. 2012, A&A, 537, A107
- Schlegel, D. J., Finkbeiner, D. P., & Davis, M. 1998, ApJ, 500, 525
- Schmidt-Kaler, T. 1982, in Landolt-Borstein, New Series, Group VI, vol. 2, eds. K. Schaifers, & H. H. Voigt (Berlin: Springer-Verlag), 1
- Schnurr, O., Moffat, A. F. J., St-Louis, N., Morrell, N. I., & Guerrero, M. A. 2008, MNRAS, 389, 806
- Shara, M. M., Moffat, A. F. J., Gerke, J., et al. 2009, AJ, 138, 402
- Siess, L., Dufour, E., & Forestini, M. 2000, A&A, 358, 593
- de Silva, G. M., Gibson, B. K., Lattanzio, J., & Asplund, M. 2009, A&A, 500, L25
- Stetson, P. B. 1994, PASP, 106, 250
- Straižys, V., & Lazauskaitė, R. 2008, Baltic Astron., 17, 253
- Straižys, V., & Lazauskaitė, R. 2009, Baltic Astron., 18, 19
- Turner, D. G. 1976, AJ, 81, 1125
- Turner, D. G. 1989, AJ, 98, 2300
- Turner, D. G. 2011, RMxAA, 47, 127
- van der Hucht, K. A. 2001, NewAR, 45, 135
- Williams, P. M., van der Hucht, K. A., van Wyk, F., et al. 2012, MNRAS, in press
- de Wit, W. J., Testi, L., Palla, F., & Zinnecker, H. 2005, A&A, 437, 247
- Yadav, R. K. S., & Sagar, R. 2001, MNRAS, 328, 370
- Zhekov, S. A., Gagn, M., & Skinner, S. L. 2011, ApJ, 727, L17

Table 1. Observation log.

VVV field d084						VVV field d086					
UT Date	HJD-2.455e6	AM	Sng	Ell.	QG	UT Date	HJD-2.455e6	AM	Sng	Ell.	QG
29 Mar. 2010	284.092893	1.550	0.91''	0.05	A	23 Apr. 2010	309.040379	1.552	0.67''	0.08	A
29 Mar. 2010	284.093200	1.547	0.85''	0.06	A	23 Apr. 2010	309.040738	1.548	0.69''	0.09	A
7 Apr. 2010	293.088925	1.462	0.89''	0.08	C	11 May 2010	327.158628	1.269	0.76''	0.17	C
7 Apr. 2010	293.089231	1.459	0.94''	0.06	C	11 May 2010	327.158984	1.268	0.80''	0.15	C
7 Apr. 2010	293.091056	1.454	1.12''	0.07	C	12 May 2010	328.150803	1.265	0.77''	0.13	C
7 Apr. 2010	293.091364	1.451	0.92''	0.10	C	12 May 2010	328.151117	1.264	0.78''	0.11	C
7 Apr. 2010	293.093232	1.446	0.95''	0.12	C	9 Jun. 2010	356.088306	1.277	0.92''	0.19	C
7 Apr. 2010	293.093539	1.444	0.89''	0.10	C	9 Jun. 2010	356.088670	1.276	0.95''	0.25	C
11 May 2010	327.149710	1.283	0.67''	0.12	C	16 Jun. 2010	363.096838	1.317	0.76''	0.20	C
11 May 2010	327.150016	1.282	0.73''	0.14	C	16 Jun. 2010	363.097294	1.317	0.75''	0.15	C
12 May 2010	328.137896	1.275	0.84''	0.06	C	21 Jun. 2010	368.087491	1.326	0.93''	0.08	A
12 May 2010	328.138247	1.274	1.13''	0.17	C	21 Jun. 2010	368.087910	1.325	1.06''	0.03	A
8 Jun. 2010	355.964570	1.328	0.91''	0.08	C	13 Jul. 2010	390.036517	1.346	0.79''	0.09	C
8 Jun. 2010	355.964937	1.326	0.93''	0.14	C	13 Jul. 2010	390.036977	1.346	0.80''	0.05	C
16 Jun. 2010	363.080558	1.326	0.74''	0.16	C	15 Aug. 2010	423.990697	1.499	0.72''	0.11	B
16 Jun. 2010	363.080968	1.325	0.73''	0.22	C	15 Aug. 2010	423.991116	1.500	0.75''	0.08	B
21 Jun. 2010	368.063868	1.320	0.92''	0.11	C	17 Aug. 2010	425.010078	1.607	0.69''	0.07	A
21 Jun. 2010	368.064288	1.319	0.95''	0.12	C	17 Aug. 2010	425.010549	1.609	0.74''	0.08	A
8 Jul. 2010	385.063093	1.439	0.76''	0.07	B	15 May 2011	696.219013	1.402	0.60''	0.13	A
8 Jul. 2010	385.063579	1.439	0.77''	0.05	B	15 May 2011	696.219447	1.402	0.57''	0.11	A
9 Jul. 2010	386.054580	1.419	0.62''	0.13	A	16 Jul. 2011	758.067592	1.464	1.15''	0.11	C
9 Jul. 2010	386.055029	1.420	0.57''	0.08	A	16 Jul. 2011	758.068015	1.465	1.22''	0.09	C
10 Jul. 2010	387.063990	1.462	0.60''	0.12	A	30 Jul. 2011	772.017268	1.420	0.69''	0.05	A
10 Jul. 2010	387.064418	1.462	0.64''	0.11	A	30 Jul. 2011	772.017713	1.421	0.73''	0.13	A
10 Aug. 2010	418.007474	1.588	0.79''	0.19	A	31 Jul. 2011	773.009639	1.404	1.37''	0.07	N/A
10 Aug. 2010	418.007953	1.589	0.79''	0.14	A	31 Jul. 2011	773.010068	1.405	1.35''	0.08	N/A
14 Jun. 2011	726.145651	1.502	0.73''	0.07	A	2 Aug. 2011	775.013248	1.435	2.30''	0.19	C
14 Jun. 2011	726.146109	1.502	0.78''	0.07	A	2 Aug. 2011	775.013651	1.435	2.02''	0.20	C
24 Jul. 2011	766.025934	1.460	0.74''	0.10	A	4 Aug. 2011	777.022491	1.491	0.77''	0.11	B
24 Jul. 2011	766.026379	1.460	0.75''	0.06	A	4 Aug. 2011	777.022898	1.492	0.70''	0.10	B
7 Aug. 2011	780.991745	1.486	0.80''	0.13	A	15 Aug. 2011	788.017516	1.614	0.85''	0.09	B
7 Aug. 2011	780.992151	1.487	0.88''	0.09	A	15 Aug. 2011	788.017933	1.616	0.76''	0.07	B
16 Aug. 2011	789.979686	1.541	0.88''	0.14	A	17 Aug. 2011	790.993083	1.531	1.16''	0.07	N/A
16 Aug. 2011	789.980120	1.542	0.96''	0.04	A	17 Aug. 2011	790.993548	1.532	1.19''	0.05	N/A
						21 Aug. 2011	794.993380	1.587	0.88''	0.11	A
						21 Aug. 2011	794.993802	1.588	0.90''	0.05	A
						22 Aug. 2011	795.995700	1.615	1.56''	0.05	C
						22 Aug. 2011	795.996109	1.616	1.61''	0.09	C

Notes. Columns include UT date, HJD-2.455e6, airmass, seeing in arcsec, ellipticity and quality grade provided by ESO. Both the d084 and d086 fields are presented.

Table 5. List of variable candidates in Danks 1 and Danks 2.

Catalogue number	RA (J2000)	Dec (J2000)	Mean(K_s)	$\log \sigma_{K_s}$	Catalogue number	RA (J2000)	Dec (J2000)	Mean(K_s)	$\log \sigma_{K_s}$
D1-0078	198.07936	-62.706541	15.86	-0.80	D1-3546	198.12989	-62.701732	16.08	-0.89
D1-0093	198.07970	-62.705462	15.20	-1.25	D1-3548	198.13037	-62.713030	14.07	-1.08
D1-0093	198.08006	-62.705399	15.79	-0.85	D1-3540	198.13098	-62.697912	14.45	-1.10
D1-0128	198.08058	-62.705065	15.86	-0.90	D1-3542	198.13103	-62.700520	13.72	-1.21
D1-0119	198.08075	-62.705865	16.28	-0.72	D1-3550	198.13485	-62.690548	18.83	-0.08
D1-0112	198.08141	-62.707093	16.96	-0.25	D1-3546	198.13841	-62.701339	11.53	-1.44
D1-0276	198.08377	-62.696737	14.32	-1.11	D1-3548	198.13906	-62.711442	17.82	-0.03
D1-0353	198.08523	-62.701102	16.22	-0.91	D1-3544	198.13994	-62.704730	14.52	-1.16
D1-0365	198.08536	-62.693862	13.07	-1.14	D1-3542	198.14063	-62.700532	14.78	-1.00
D1-0379	198.08566	-62.704213	14.23	-0.95	D1-3538	198.14074	-62.709018	17.69	-0.24
D1-0520	198.08913	-62.710759	18.51	-0.29	D1-3538	198.14216	-62.709617	16.76	-0.28
D1-0605	198.09067	-62.704842	16.60	-0.74	D1-3548	198.14252	-62.710469	17.49	-0.10
D1-0624	198.09105	-62.699257	17.31	-0.52	D1-3538	198.14332	-62.709620	15.35	-0.71
D1-0629	198.09112	-62.703998	13.27	-1.72	D1-3538	198.14337	-62.708983	16.79	-0.38
D1-0719	198.09152	-62.707777	16.73	-0.67	D1-3544	198.14476	-62.705129	16.82	-0.55
D1-0792	198.09356	-62.712184	16.35	-0.59	D2-0007	198.19466	-62.686308	15.91	-0.84
D1-0823	198.09395	-62.707737	11.97	-0.82	D2-0045	198.19639	-62.682487	17.74	-0.45
D1-0840	198.09415	-62.692784	14.85	-1.07	D2-0061	198.19709	-62.684371	14.04	-1.11
D1-0848	198.09432	-62.709843	17.63	-0.14	D2-0187	198.20026	-62.678689	13.91	-1.22
D1-0871	198.09473	-62.702318	12.60	-1.09	D2-0266	198.20216	-62.675668	17.65	-0.37
D1-1124	198.09827	-62.697101	17.24	-0.51	D2-0342	198.20354	-62.679100	18.57	-0.05
D1-1125	198.09835	-62.703466	14.83	-1.05	D2-0383	198.20495	-62.670688	17.25	-0.26
D1-1295	198.10051	-62.703707	14.17	-1.05	D2-0415	198.20523	-62.672838	16.06	-0.88
D1-1328	198.10091	-62.716417	16.51	-0.94	D2-0658	198.20920	-62.672609	17.60	-0.24
D1-1506	198.10326	-62.696218	12.64	-1.30	D2-0992	198.21392	-62.666613	12.98	-0.93
D1-1808	198.10722	-62.700764	13.88	-1.08	D2-1063	198.21452	-62.683190	17.99	-0.38
D1-1941	198.10898	-62.700922	14.09	-1.16	D2-1519	198.22076	-62.677181	17.48	-0.31
D1-2062	198.11031	-62.714601	17.02	-0.50	D2-1597	198.22225	-62.689244	14.71	-1.20
D1-2350	198.11371	-62.696060	12.40	-1.10	D2-1862	198.22601	-62.682288	13.30	-0.81
D1-2413	198.11389	-62.697167	17.80	-0.11	D2-2029	198.22850	-62.679058	14.63	-1.18
D1-2379	198.11411	-62.717062	15.75	-1.04	D2-2182	198.23048	-62.682038	15.86	-1.09
D1-2397	198.11427	-62.687730	16.35	-0.86	D2-2223	198.23107	-62.674319	13.55	-1.28
D1-2408	198.11439	-62.688650	12.16	-1.60	D2-2299	198.23172	-62.677520	17.72	-0.37
D1-2468	198.11514	-62.712483	15.87	-0.92	D2-2289	198.23204	-62.694124	15.18	-1.00
D1-2763	198.11776	-62.708380	18.45	-0.32	D2-2497	198.23481	-62.677910	15.51	-0.84
D1-2801	198.11893	-62.708093	13.48	-1.51	D2-2528	198.23522	-62.670558	17.24	-0.28
D1-2879	198.11967	-62.699463	14.46	-1.27	D2-2548	198.23541	-62.671228	16.95	-0.29
D1-2974	198.12079	-62.692725	15.02	-0.77	D2-2579	198.23612	-62.694739	17.22	-0.53
D1-2974	198.12110	-62.692668	15.38	-1.13	D2-2599	198.23641	-62.683018	14.71	-1.39
D1-3016	198.12155	-62.707313	18.52	-0.14	D2-2603	198.23733	-62.690218	12.91	-1.55
D1-3135	198.12340	-62.692690	17.57	-0.17	D2-2783	198.23950	-62.675108	12.78	-1.49
D1-3361	198.12551	-62.701561	17.10	-0.36	D2-2824	198.24012	-62.667779	16.29	-0.62
D1-3465	198.12752	-62.697527	13.99	-1.46	D2-3128	198.24442	-62.694468	18.28	-0.19
D1-3491	198.12779	-62.692769	16.12	-0.60	D2-3203	198.25360	-62.692373	16.44	-0.46
D1-3554	198.12955	-62.702017	17.23	-0.18					

Notes. Columns include RA (J2000), Dec (J2000), Mean (K_s) and $\log \sigma_{K_s}$.

Table 6. List of variable candidates in RCW 79.

Catalogue number	RA (J2000)	Dec (J2000)	Mean(K_s)	$\log \sigma_{K_s}$	Catalogue number	RA (J2000)	Dec (J2000)	Mean(K_s)	$\log \sigma_{K_s}$
RCW79-0029	204.94346	-61.753372	14.71	-1.42	RCW79-0445	204.98517	-61.742081	18.54	-0.21
RCW79-0040	204.94577	-61.759210	18.17	-0.13	RCW79-0477	204.98628	-61.750475	15.93	-1.08
RCW79-0002	204.94651	-61.744302	18.04	-0.42	RCW79-0520	204.98716	-61.744896	17.09	-0.27
RCW79-0002	204.95280	-61.738925	17.48	-0.25	RCW79-0548	204.98786	-61.746405	17.16	-0.36
RCW79-0029	204.95483	-61.745262	17.68	-0.32	RCW79-0634	204.98923	-61.744089	16.33	-0.43
RCW79-0002	204.95519	-61.737823	17.77	-0.53	RCW79-0641	204.98962	-61.750225	15.85	-0.81
RCW79-0029	204.96003	-61.746189	17.58	-0.04	RCW79-0669	204.99144	-61.750221	17.58	-0.41
RCW79-0029	204.96382	-61.742056	15.94	-0.68	RCW79-0748	204.99336	-61.736630	18.04	-0.14
RCW79-0150	204.96390	-61.755874	17.87	-0.48	RCW79-0847	204.99354	-61.748245	17.95	-0.31
RCW79-0002	204.97027	-61.734321	16.02	-1.00	RCW79-0886	204.99462	-61.736643	18.34	-0.17
RCW79-0131	204.97211	-61.747668	18.14	-0.18	RCW79-1028	204.99670	-61.752871	16.31	-0.92
RCW79-0150	204.97213	-61.754339	17.03	-0.72	RCW79-0982	204.99693	-61.741871	16.89	-0.17
RCW79-0150	204.97408	-61.754537	17.26	-0.46	RCW79-1019	204.99724	-61.756554	11.96	-0.96
RCW79-0071	204.97458	-61.741244	18.09	-0.27	RCW79-0991	204.99758	-61.740530	15.62	-0.99
RCW79-0176	204.97811	-61.742926	17.79	-0.09	RCW79-1088	204.99809	-61.741124	18.03	-0.04
RCW79-0235	204.97847	-61.750456	18.17	-0.18	RCW79-1056	204.99852	-61.747515	17.90	-0.14
RCW79-0330	204.98300	-61.737352	16.47	-0.79	RCW79-1207	205.00134	-61.750141	17.62	-0.31
RCW79-0394	204.98390	-61.736090	16.39	-0.85	RCW79-1399	205.00368	-61.743272	17.41	-0.14

Notes. Columns include RA (J2000), Dec (J2000), Mean (K_s) and $\log \sigma_{K_s}$.